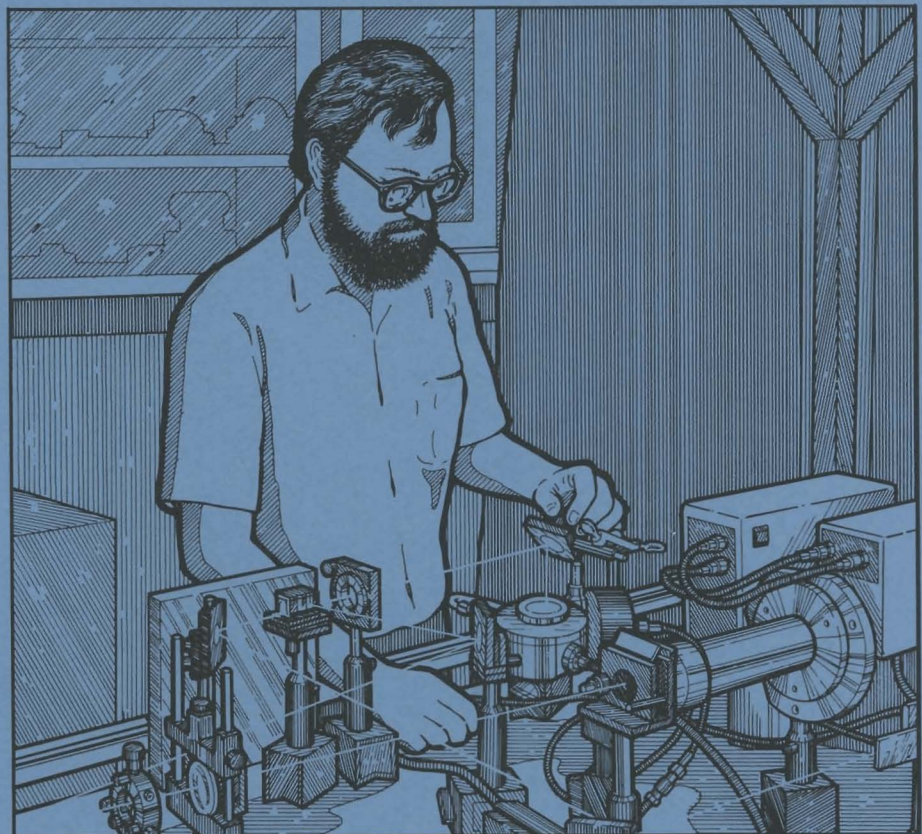


# LLE Review

## Quarterly Report



January–March 1988

Laboratory for Laser Energetics  
College of Engineering and Applied Science  
University of Rochester  
250 East River Road  
Rochester, New York 14623-1299



# LLE Review

## Quarterly Report

*Editor:* J. Kelly  
(716) 275-4710

January–March 1988

---

Laboratory for Laser Energetics  
College of Engineering and Applied Science  
University of Rochester  
250 East River Road  
Rochester, New York 14623-1299



This report was prepared as an account of work conducted by the Laboratory for Laser Energetics and sponsored by Empire State Electric Energy Research Corporation, New York State Energy Research and Development Authority, Ontario Hydro, the University of Rochester, the U.S. Department of Energy, and other United States government agencies.

Neither the above named sponsors, nor any of their employees, makes any warranty, expressed or implied, or assumes any legal liability or responsibility for the accuracy, completeness, or usefulness of any information, apparatus, product, or process disclosed, or represents that its use would not infringe privately owned rights.

Reference herein to any specific commercial product, process, or service by trade name, mark, manufacturer, or otherwise, does not necessarily constitute or imply its endorsement, recommendation, or favoring by the United States Government or any agency thereof or any other sponsor.

Results reported in the LLE Review should not be taken as necessarily final results as they represent active research. The views and opinions of authors expressed herein do not necessarily state or reflect those of any of the above sponsoring entities.

## IN BRIEF

This volume of the LLE Review, covering the period January–March 1988, contains articles on the spectra of scattered laser radiation from laser-produced plasmas and on the bounce coating of ablation layers on fusion targets. The advanced technology section has reports on a novel technique for characterizing surface breakdown on semiconductor devices and on a versatile alexandrite regenerative amplifier. Finally, the activities of the National Laser Users Facility and the GDL and OMEGA laser facilities are summarized.

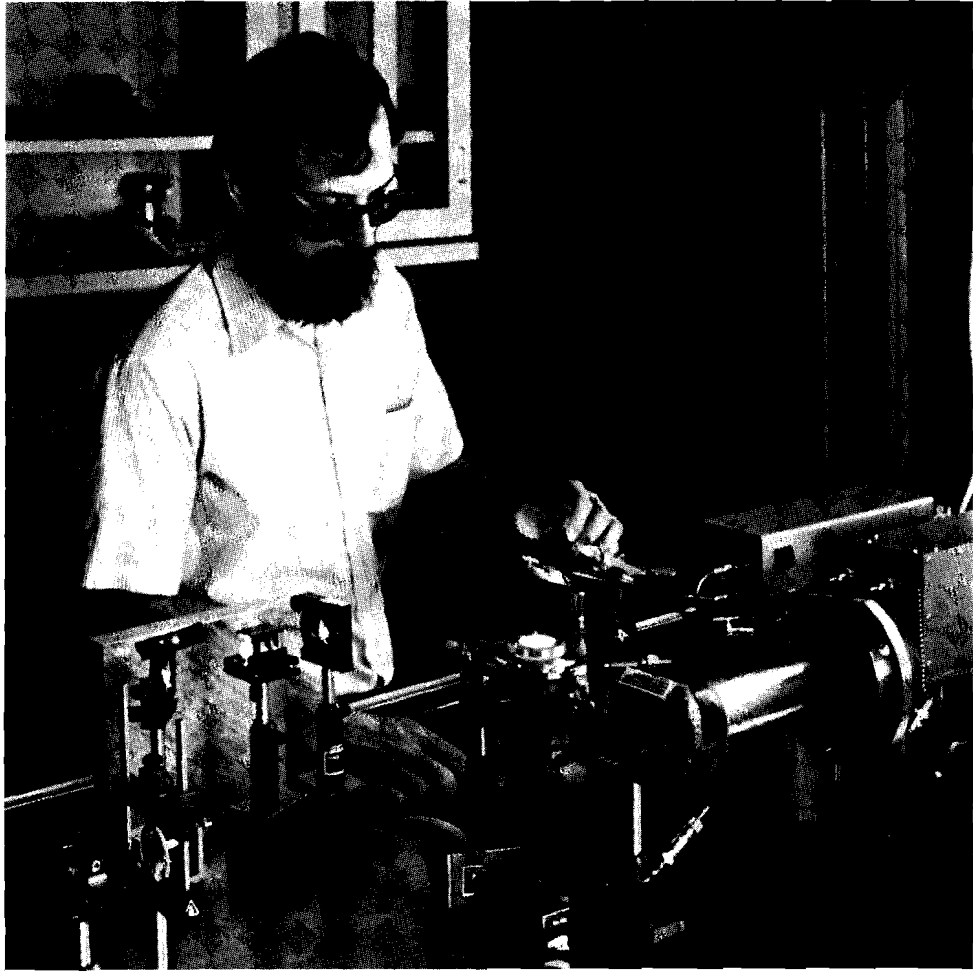
The highlights of this issue are

- A systematic study of the scattered-light spectrum from a laser-produced plasma has observed features both above and below  $3\omega_0/2$ , as well as between the laser frequency ( $\omega_0$ ) and its half-harmonic. All of these features can be self-consistently interpreted in terms of enhanced Thomson scattering.
- A careful parameter study has optimized the process control parameters in the plasma-assisted bounce coating of parylene ablation layers on fusion targets. The high tensile strength coatings obtained with this technique allow high fuel pressures in polymer shell targets.
- An electro-optic crystal placed in the fringing fields above a semiconductor device was probed with a large-area, short optical pulse. The modulated optical pulse was imaged onto a detector array to produce a map of the surface fields and information about semiconductor surface breakdown.

- A tunable alexandrite regenerative amplifier has been used to amplify pulses from such diverse sources as a picosecond gain-switched laser diode, a synch-pumped femtosecond dye laser, and the nanosecond-sliced output of a cw dye laser, while retaining the temporal and spectral characteristics of each source.

# CONTENTS

	<i>Page</i>
IN BRIEF .....	iii
CONTENTS .....	v
Section 1 PROGRESS IN LASER FUSION .....	49
1.A Observations of Enhanced Thomson Scattering .....	49
1.B Bounce-Coated Ablation Layers on Fusion Targets .....	66
Section 2 ADVANCED TECHNOLOGY DEVELOPMENTS .....	74
2.A Optical Probes for the Characterization of Surface Breakdown .....	74
2.B Regenerative Amplification in Alexandrite of Pulses from Specialized Oscillators .....	84
Section 3 NATIONAL LASER USERS FACILITY NEWS .....	93
Section 4 LASER SYSTEM REPORT .....	95
4.A GDL Facility Report .....	95
4.B OMEGA Facility Report .....	96
PUBLICATIONS AND CONFERENCE PRESENTATIONS	



William Donaldson, a scientist in the Ultrafast Science Division, adjusts the optical alignment of the surface electric field imaging system.

# Section 1

## PROGRESS IN LASER FUSION

### 1.A Observations of Enhanced Thomson Scattering

The scattered-light spectrum from a laser-produced plasma includes several frequently observed features, such as the even and odd half-harmonics of the laser frequency. These features are fairly well understood and can be explained in terms of parametric instabilities or resonance absorption. We have, however, found three large spectral features that are not easily explained in terms of parametric instabilities. One lies between the laser frequency ( $\omega_0$ ) and its half-harmonic ( $\omega_0/2$ ) and will be referred to here as the down-scattered band. The other two are up-scattered bands near  $3\omega_0/2$ , one above this value and one below.

These features can be explained by an enhanced Thomson scattering (ETS) model.<sup>1-3</sup> Briefly, these enhanced scattering bands arise from Thomson scattering of the pump laser on density variations that have been enhanced by the presence of pulses of fast electrons.

This model has three parameters, which determine the position of a scattering band: the background ("cold") electron temperature; the central directed velocity of the fast-electron pulse; and the relative numbers of fast electrons in the pulse. The directed velocity can be inferred from a time-integrated measurement of a hot-electron "temperature." Experiments were conducted to independently measure the location of the scattering bands and the hot- and cold-electron temperatures.

Previous experiments<sup>4,5</sup> concentrated on the down-scattering feature, on the supposition that it is the signature for the convective stimulated Raman scattering (SRS) instability. A recent paper<sup>6</sup> observed both up- and down-scattered bands and explained the presence of the up-scattered band as due to anti-Stokes mixing.

### Theory

The SRS instability occurs as a result of the coupling of a scattered electromagnetic (EM) wave, with a fluctuation in a plasma wave through the presence of an oscillating EM pump wave. An initial-density perturbation (noise) produces a transverse current due to the oscillatory pump wave, which in turn produces a reflected EM wave. The ponderomotive force of the interacting incident and reflected EM waves enhances the initial-density perturbations.<sup>7</sup> This feedback mechanism will amplify any initial noise (plasma-wave amplitude) exponentially until the instability saturates by convection or by some nonlinear process. To initiate this cycle, the pump wave must be strong enough to overcome any losses in this system, including convection and damping of the waves. Therefore, a threshold pump power (i.e., threshold laser intensity) will exist for SRS.

Even below the threshold for the SRS instability, there will still be low-level scattering of EM light by interaction of the pump wave with collective thermal fluctuations in the plasma. This scattered EM light is what is called the “electron line feature” of classical Thomson scattering. As long as the plasma waves are at thermal levels, the fractional energy scattered this way is quite small. If for some reason the electron distribution deviates significantly from Maxwellian, however, considerable enhancement of some of the plasma-wave levels may exist. In such a case, enhancement of the Thomson scattering may occur and could easily be mistaken for a signature of SRS.

Even when the SRS threshold is exceeded, the exponential growth proceeds from the initial noise level. Those plasma densities at which enhanced plasma-wave levels exist contribute most efficiently to the SRS signal; thus, this enhanced “seed” may still determine the frequency spectrum of the observable Raman scattering.

For a given plasma density, the scattered light and plasma waves must satisfy the following energy and momentum matching conditions for the SRS instability to occur:

$$\begin{aligned}\omega_0 &= \omega_s + \omega_p \\ k_0 &= k_s + k_p \quad ,\end{aligned}\tag{1}$$

where  $\omega_0$  ( $k_0$ ),  $\omega_s$  ( $k_s$ ), and  $\omega_p$  ( $k_p$ ) are the frequencies (wave vectors) of the laser, scattered-light wave, and plasma wave, respectively. In addition, the scattered EM and plasma waves must satisfy the relevant dispersion relations:

$$\begin{aligned}\omega_0^2 &= \omega_{pe}^2 + c^2 k_0^2 \\ \omega_s^2 &= \omega_{pe}^2 + c^2 k_s^2 \\ \omega_p^2 &= \omega_{pe}^2 + 3v_T^2 k_p^2 \quad ,\end{aligned}\tag{2}$$

where  $\omega_{pe}$  is the plasma frequency,  $c$  is the speed of light, and  $v_T$  is the electron thermal velocity. Taken together, Eqs. (1) and (2) imply that the frequency of the scattered light is proportional to the plasma density at its origin and that the scattered SRS EM wave may occur only in the frequency interval<sup>8</sup>  $\omega_0/2 < \omega_s < \omega_0$ . The threshold for convective SRS (SRS-C) in an inhomogeneous plasma is given by<sup>9</sup>

$$\left(\frac{v_o}{c}\right)^2 k_o L > 1, \quad (3)$$

where  $v_o$  is the electron oscillatory velocity,  $k_o$  is the laser wave number inside the plasma, and  $L$  is the plasma scale length. In practical units, the threshold condition on the incident intensity may also be written as

$$I_{\text{thres}} = \frac{4.4 \times 10^{17}}{L_\mu \lambda_\mu} \frac{\text{W}}{\text{cm}^2}, \quad (4)$$

with  $L_\mu$  and  $\lambda_\mu$  expressed in microns. In our experiments,<sup>10</sup>  $\lambda_\mu = 0.527$  and  $L_\mu \sim 80$ , corresponding to an intensity threshold of  $1 \times 10^{16} \text{ W/cm}^2$ .

Enhanced Thomson scattering, in contrast, has no threshold as such, but does require an electron distribution that is non-Maxwellian. The theory in Ref. 1 assumes that bursts of energetic electrons are produced at the quarter-critical density surface by the onset of parametric instabilities, such as absolute stimulated Raman scattering (SRS-A)<sup>11</sup> and two-plasmon decay (TPD).<sup>12</sup> At the critical surface, resonance absorption (RA), although not a parametric instability, can also produce energetic electrons.<sup>13</sup> These bursts move out into the plasma and can be reflected at sheaths. Locally, this produces a transient, "bump-on-tail" electron velocity distribution if the number of hot electrons exceeds some minimum value. Because of the subsequent isotropization and slowing of these fast electrons, any time-integrated measurement of their x rays can be interpreted in terms of an effective "hot"-electron temperature  $T_h$ . According to the theory in Ref. 1, this temperature is related to the initial directed velocity of the burst,  $v_d$ , by  $mv_d^2 = 3kT_h$ . We expect that the time-integrated x-ray spectrum of our plasma can be interpreted in terms of a cold-electron temperature  $T_c$ , corresponding to the background thermal electrons; plus a hot component  $T_h$  from RA (if present); and a "superhot" component  $T_{sh}$  from SRS-A and TPD. For the conditions in our experiments, the cold temperature is typically between 0.8 and 2 keV, the hot temperature is between 5 and 10 keV, and the superhot temperature can range between 15 and 60 keV. Most of the electrons are in the cold component.

If it is assumed that the fast-electron bursts move up and down along the direction of the density gradient, it is possible to calculate the resulting enhanced Thomson scattering. Computer calculations show that the enhanced scattering in an inhomogeneous plasma will occur in two bands: one, a down-scatter band between  $\omega_0$  and  $\omega_0/2$ ; the other, an up-scatter band between  $2\omega_0$  and  $\omega_0$ . The two bands are not symmetrical about  $\omega_0$ , nor need they have the same minimum

number of fast electrons (i.e., the same threshold) for the enhancement to occur.

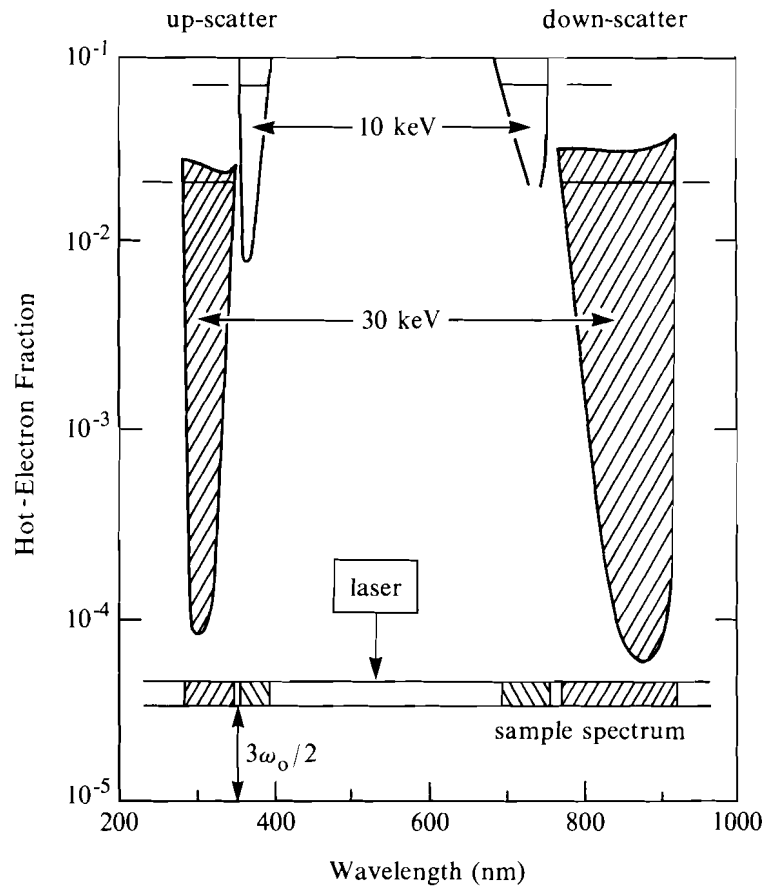
If there are two distinct hot temperatures identified in an experiment, a second pair of enhanced bands is expected to be present. However, the minimum number of hot electrons required may vary considerably from band to band, and so not every band need be observed in any given experiment.

Of course, the spectral location and width of the bands are also functions of three variables: the angle of incidence of the laser relative to the density gradient, the angle of observation, and the average ionic charge. All these variables have been included in a numerical calculation. The result is usually insensitive to the value of  $T_c$ , and the central location of the band does not vary appreciably when the fraction of hot electrons is increased above some minimum value.

An example of a simulated spectrum for the conditions of this experiment, including refraction, is shown in Fig. 34.1, where the enhanced wavelength bands are shown as a function of  $f_h$ , the fraction of directed hot electrons in the pulse relative to the background density. This calculation assumed a tilted target at  $45^\circ$ , a laser wavelength of  $\lambda_o = 527$  nm, an average ionic charge of  $Z = 3$ , a cold temperature of  $T_c = 1.5$  keV, and a typical superhot temperature of 30 keV. There is as yet no reliable theory that will predict the number of hot electrons; hence,  $f_h$  is unknown. Fortunately, the central location of each band is insensitive to the value of  $f_h$ . As an example, if the superhot electron fraction  $f_{sh}$  is equal to 1%, Fig. 34.1 then predicts an up-scattered band between 286 and 350 nm and a down-scattered band between 777 and 920 nm. Note that this theory naturally predicts a gap between the long-wavelength limit of the down-scattered feature and the half-harmonic at 1054 nm. Also noteworthy is that the up-scattering feature extends well below the three-halves harmonic.

Figure 34.1 also shows the additions to the predicted spectrum if a third temperature, the hot component, is present. An additional pair of bands is added. As an example, for a hot temperature of 10 keV and a hot-electron fraction of 8%, there will be up-scattering between 360 and 400 nm, on the long-wavelength side of the three halves, and down-scattering between 690 and 760 nm. We would have observed a four-peaked spectrum if a large fraction of the electrons had been in the hot and superhot components.

There are several points in Fig. 34.1 that will be useful to note when interpreting experimental results. First, the down-scattering signals can be easily confused with the signal from SRS-C, since it also occurs between  $\omega_o/2$  and  $\omega_o$ . Furthermore, the short-wavelength cutoff is at about the same wavelength because its basic cause, Landau damping, is the same for both SRS-C and ETS. Various theories have been proposed to explain the long-wavelength gap near  $\omega_o/2$  in SRS. These explanations include density steepening and suppression by ion waves, but none of these are quantitative as yet. Therefore, if only the down-



E4408

Fig. 34.1  
 Predicted enhanced Thomson scattering bands as observed in the direction normal to the target, assuming a three-component temperature distribution with  $T_c = 1.5$ ,  $T_h = 10$ , and  $T_{sh} = 30$  keV. The target is tilted at  $45^\circ$  and has  $Z = 3$ . The laser wavelength is 527 nm.

scattered signal is measured, SRS-C and ETS are difficult to distinguish. In addition, the superhot-electron fraction threshold for down-scattering is much lower than that for scattering caused by hot electrons. It is entirely possible that only the superhot down-scattering band will be observed. Finally, while the superhot-electron fraction threshold for down-scattering is lower than that for up-scattering, the reverse is true for the hot features. In fact, the hot up-scatter threshold is less than half that for the hot down-scatter threshold. It is therefore possible that there are enough hot electrons to produce the up-scattering band but not enough to produce the corresponding down-scattering band.

### Experiments

A series of experiments using the glass development laser (GDL) system<sup>14</sup> at LLE was conducted to observe the anomalous scattering bands. GDL is a single-beam Nd:glass system that, for this series of experiments, delivered up to 200 J at  $1.054 \mu\text{m}$ . Frequency doubling produced on-target energies of up to 60 J at 527 nm. The pulses were Gaussian in time and usually had a pulse width of approximately 600 ps after frequency conversion, although some experiments were done

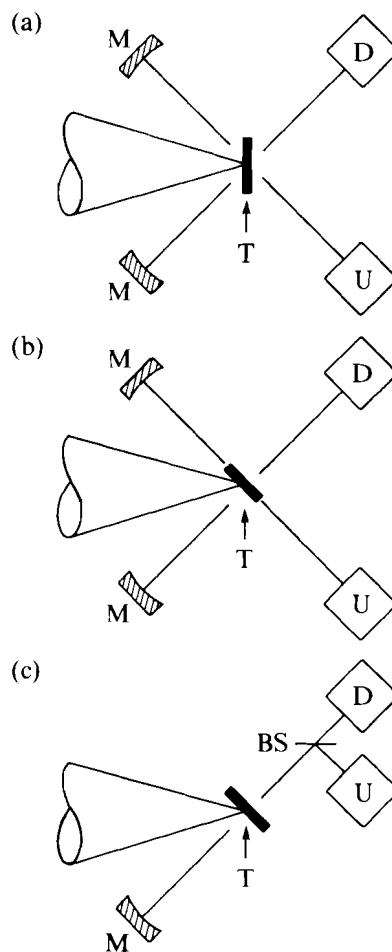
with 1-ns pulses. The beam was focused onto 50- $\mu\text{m}$ -thick Mylar targets by an  $f/3.6$  lens. The x-ray spot size at 10% of the maximum intensity, as measured by an aluminum and beryllium-filtered pinhole camera, was 120  $\mu\text{m}$  at best focus. This corresponds to a maximum average on-target intensity of  $8 \times 10^{14} \text{ W/cm}^2$ .

Precautions were taken to limit the amount of blue (third-harmonic) and red (fundamental) energy on target. Residual 1.054- $\mu\text{m}$  light intensity was reduced by the use of an IR absorber plate, dichroic mirrors, and by the chromatic shift of the focusing lens, resulting in  $I_{1054 \text{ nm}} = 10^{-9} I_{527 \text{ nm}}$ .

Scattered light was collected by two spherical aluminum mirrors each subtending a solid angle of 0.087 sr and focused onto the entrance slits of two, 0.25-m spectrometers. The first (UV) spectrometer, which incorporated a cross Czerny-Turner design with a 275-mm focal length and used a 600-groove/mm grating blazed at 300 nm, was usually tuned to observe the spectrum between 250 and 425 nm in order to view the up-scattered feature; the spectrum was recorded on Kodak 2495 film, with a resolution of better than 1 nm. The second (IR) spectrometer, which was used to view the down-scatter at wavelengths longer than 600 nm, was a quarter-meter Ebert monochromator equipped with a 170-groove/mm grating blazed at 500 nm. When used to view the time-integrated down-scatter, as in the first geometry [Fig. 34.2(a)], the signal was recorded on Kodak 4143 high-speed IR film. The spectral range was limited on the long-wavelength side to 925 nm by the falloff in film response. The short-wavelength side was limited to 570 nm by the use of sharp-cut, long-pass filters to reduce stray 527-nm light.

Three target/observation geometries were used. The first [Fig. 34.2(a)] had the laser normally incident onto the target and the mirrors placed at  $135^\circ$  from the forward direction. In this case, the two spectrometers were sampling the same observation angle. The second geometry [Fig. 34.2(b)] had the target tilted at  $45^\circ$ . The collection mirrors were at the same angles with respect to the laser so that the down-scattered spectrum was collected from the direction normal to the target and the up-scattered spectrum was observed along the target face ( $90^\circ$  sidescatter). The third geometry [Fig. 34.2(c)] employed a similarly tilted target, but only one collection mirror was used, sampling along the target normal. The scattered light was directed onto the down-scatter spectrometer. A portion of this light was split off by an uncoated microscope slide that acted as a 4%-per-surface beamsplitter. Only the front surface reflectance was directed onto the up-scatter spectrometer. The use of an aluminized 10% beamsplitter in place of the uncoated glass reduced the down-scatter signal below detectable levels.

The IR spectra was also time resolved for all three geometries (Fig. 34.3). The output of the IR spectrometer was focused onto a streak camera slit by a pair of lenses: first, a cylindrical field lens with a 400-mm focal length used to collimate the spectrometer output, and second, a convex lens with a 43-mm focal length. The streak camera



E4463

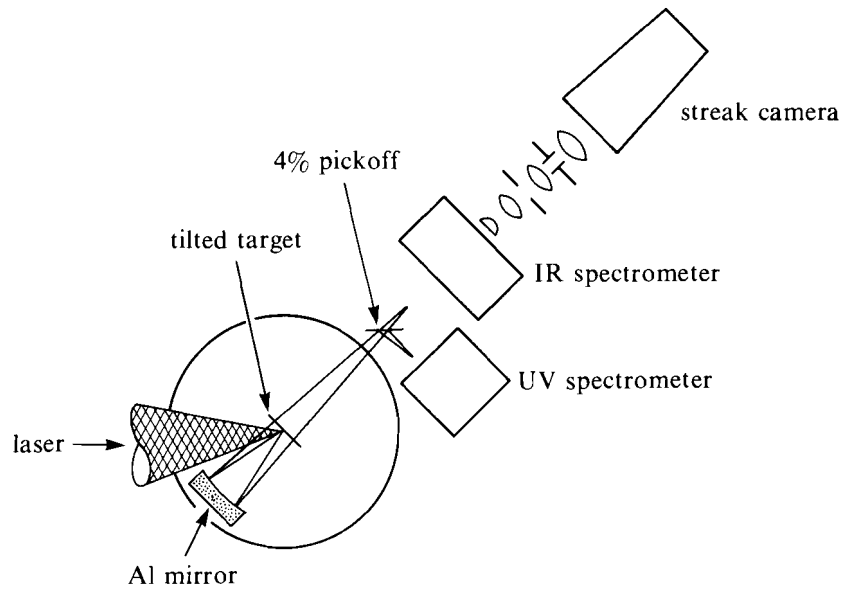
Fig. 34.2

Three detector/target geometries were used in the experiment. The scattered light is collected by two aluminium mirrors and focused onto the spectrometer slits with an effective  $f$  number of 13. In (a), both the up- and down-scattering signals are observed at  $135^\circ$  from the direction of laser propagation. In (b), the target was tilted at  $45^\circ$  to the laser with the observation angles unchanged. In (c), signals were sampled in the direction of the tilted target normal. The mirrors are labeled by  $M$ , the up-scattering (UV) spectrometer by  $U$ , the down-scattering (IR) spectrometer by  $D$ , the beamsplitter by  $BS$ , and the target by  $T$ .

and spectrometer slits were crossed to give both time and spectral resolution. The optics between the streak camera slit and the photocathode were corrected so that the effects of chromatic shifts were reduced.

An Imacon 675 streak camera equipped with an S-1 tube whose response peaked at 750 nm and fell off rapidly to either side, becoming ten times less sensitive at  $1.05 \mu\text{m}$ , was used. The S-1 tube was very old and its sensitivity to  $1\text{-}\mu\text{m}$  light has degraded to an even lower sensitivity. Streak data were taken at a sweep speed of 100 ps/mm. Due to the finite size of the photocathode, the spectral window was limited to 450 nm with a resolution of 10 nm.

The dispersion of the spectrometer/streak camera combination was determined by directing the output of two HeNe lasers, operating at wavelengths of 628 and 543.5 nm, onto the spectrometer slit. The grating was set so that the first-order red and second-order green and



E4405

Fig. 34.3

Schematic layout for measuring the time-resolved down-scattering spectra. The optics between the streak camera slit and the photocathode were wavelength corrected to reduce chromatic distortion. The up-scattered signal was split off from the down-scattered by an uncoated glass slide.

red lines could be seen on the streak camera image intensifier phosphor when in focus mode. For an absolute wavelength fiducial, the IR absorber plate was removed from the incident laser beam, the lens was defocused, and low-energy ( $\ll 1$ -J) shots on gold targets, tilted at  $22.5^\circ$ , were taken to record the unconverted fundamental laser line. This also gave a temporal dispersion measurement. The data was recorded on Kodak Tri-X film, which was push processed to an equivalent ASA of at least 4,000.<sup>15</sup>

To determine the electron temperature, the x-ray continuum from the target was measured and a two- or three-Maxwellian electron distribution was fit to it.<sup>16</sup> The x-ray detectors consisted of nine PIN diodes and six scintillator-photomultiplier tube units filtered with various K-edge filters. In this experiment, the best results were obtained assuming a two-temperature model with cold and superhot temperature components. The former is characteristic of the dense plasma above  $n_c$ , while the latter is characteristic of nonlinear processes involving plasma waves at or below  $n_c/4$ . A third, or hot, component, which is characteristic of interaction phenomena near  $n_c$  (resonance absorption and/or the parametric decay instability) was not observed because its x-ray signal was too weak. We emphasize that this temperature measurement is independent of scattered light measurements.

## Results

We first report on the time-integrated spectra obtained using the geometry of Fig. 34.2(a). The observation angles were both  $135^\circ$ , so our observations are affected by refraction, especially in the down-scatter measurement. Figure 34.4 shows three typical spectra. As the

incident intensity is increased (which would correspond to raising the superhot electron temperature), the long-wavelength shoulder increases in intensity and its long-wavelength cutoff increases. The long-wavelength sensitivity of our data is limited because of the extremely sharp cutoff, 925 nm, of the Kodak 4143 film used.

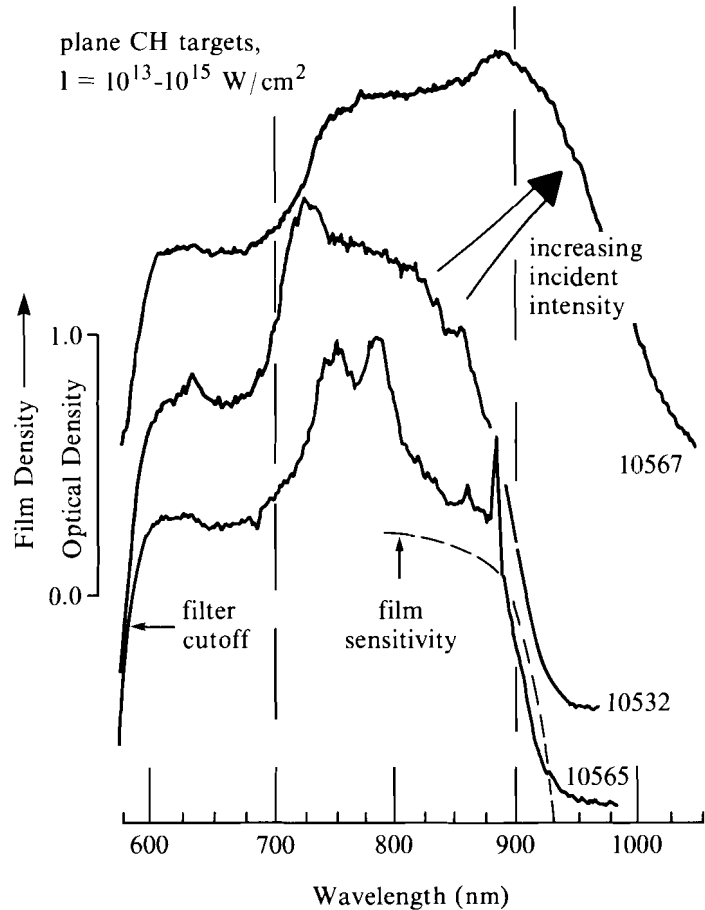
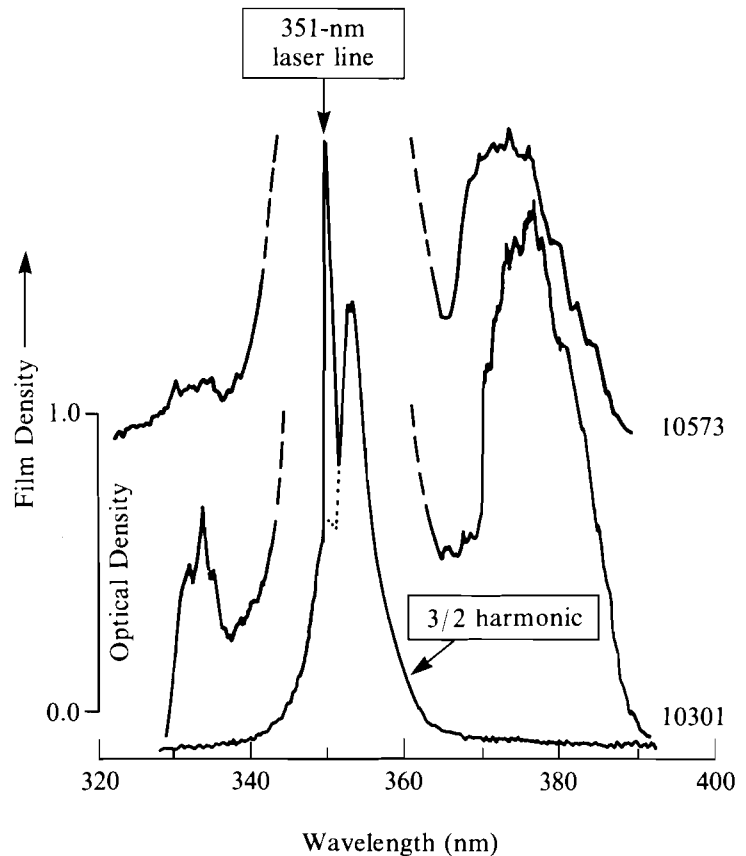


Fig. 34.4  
Time-integrated down-scattering spectra arranged in order of increasing incident intensity. The spectral window was limited to  $570 < \lambda < 925$  nm by cutoff filters at 570 nm and by the film sensitivity at 925 nm.

E4053

The best example of up-scattering, in this geometry, is shown in Fig. 34.5. The three-halves feature around 351 nm dominates the scattering bands and is itself partly blurred by residual 351-nm laser light inadvertently created in the doubling-tripling crystal assembly. In later experiments, the 351-nm laser light was completely suppressed by using the tripling (second) crystal as a doubler and detuning the first crystal. The two up-scattering features are distinctly separated from the three-halves spectrum, one to either side. If we assume that the spectra in Figs. 34.4 and 34.5 are typical and consistent, we can fit them using the enhanced Thomson scattering theory, as shown in Fig. 34.6. Since no x-ray temperature measurement was taken on these shots, we estimate the hot and superhot temperatures to be 7 and 30 keV, respectively. By choosing suitable hot-electron fractions, the observed spectra of two up-scattered peaks straddling the three-halves feature



E4465

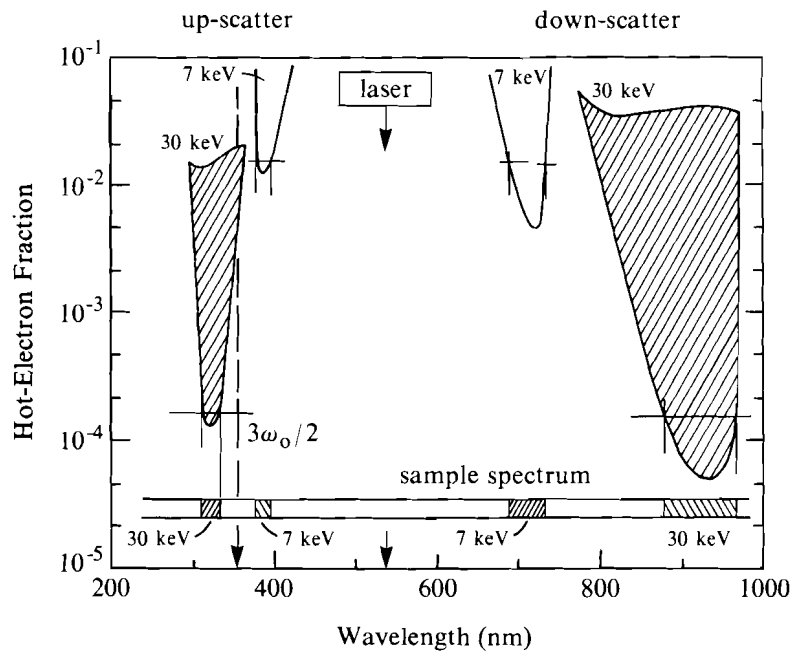
Fig. 34.5

Up-scattering spectra showing the  $3\omega_0/2$  signal and two enhanced Thomson scattering features that arise from a hot component of the electron-temperature distribution at 8 to 10 keV and a superhot component at 25 to 30 keV.

and a down-scattered feature near 700 nm can be self-consistently reproduced. The fourth predicted band, above 900 nm, was not observed due to the lack of film sensitivity, except for shot 10567, which was extremely intense and overexposed the film.

Using the same geometry, the down-scattering signal was time resolved, as shown in Fig. 34.7. The time-integrated signal shows the very narrow down-scattering observed at 900 nm and the familiar double-peaked  $\omega_0/2$  feature. Due to instrumental restrictions, we have no data below 800 nm for this series of experiments, and no attempt was made to correct the spectra for the frequency response of the detector assembly. The time-resolved picture shows that the  $\omega_0/2$  signal turns on well before the ETS signal, as expected if TPD creates the  $\omega_0/2$  signal and the superfast electrons that seed the ETS signal. The down-scattering is of very short duration—less than 200 ps—and turns itself on and off at least twice. In most of the experiments using this geometry, the  $\omega_0/2$  feature was not observed; in some, however, the down-scattering was evident and had the same temporal history.

We did not consistently observe the half-harmonic signal for three reasons. First, the  $\omega_0/2$  emission is strongly peaked in the direction of



E4051

Fig. 34.6 Predicted enhanced Thomson scattering spectral bands for electron-temperature components of 1, 7, and 30 keV. The angle of observation is  $45^\circ$ ; the target is normal to the laser and has  $Z = 3$ . Refraction of the outgoing ETS light is taken into account using a planar plasma blow-off geometry.

the density gradient, which is not the same as the direction of observation. Second, whatever  $\omega_0/2$  signal was emitted in the observed direction would be strongly refracted. Finally, since an old S-1 streak tube was used, its sensitivity to  $1\text{-}\mu\text{m}$  light was very low.

The experiments using the geometry described by Fig. 34.2(b) were less illuminating. No up-scatter signal was observed at all, primarily because the observations were at  $90^\circ$  from the density gradient. The ETS theory predicts up-scattering signals in this geometry only for  $T_{sh} > 60$  keV and then only for extremely large hot-electron fractions (of the order of 10%). The down-scattering data is similar to the following, since the down-scattering geometries were the same.

A series of experiments was conducted using the geometry depicted in Fig. 34.2(c). In this geometry, simultaneous observations were made of the up- and down-scattering in the same direction, along the target normal, which may be assumed to be the direction of the density gradient. We present two down-scattered spectra in Fig. 34.8. On both we can see the large  $\omega_0/2$  signal which, because of the choice of target orientation, is not affected by refraction. The position of the down-scattering peak is different for these two shots, even though the average intensities ( $8 \times 10^{14}$  W/cm<sup>2</sup>) and measured superhot-electron temperatures are the same. We attribute these differences to hot spots in the on-target energy distribution, which varies from shot to shot due to differences in air turbulence in the beamline. We believe that these hot spots are dominating the interaction process described here, especially in terms of the superhot-electron production and

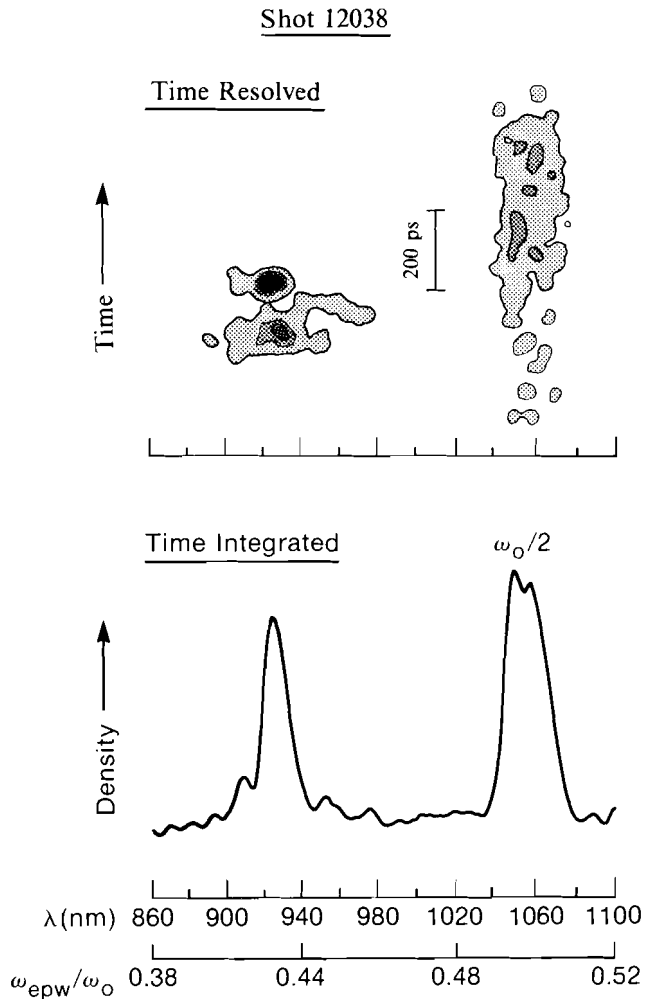


Fig. 34.7  
 Time-resolved down-scattering spectra. The average intensity was  $1 \times 10^{15}$  W/cm<sup>2</sup> in a 1-ns pulse. Note that the  $\omega_o/2$  signal turns on before the enhanced Thomson scattering signal.

E4464

consequently the enhanced Thomson scattering signal. The absence of the  $\omega_o/2$  splitting is attributed to saturation of the streak camera photocathode and the S-1 aging problem already discussed.

The temporal history of this shot, as shown in Fig. 34.9, is similar to Fig. 34.7, showing that the same process is being observed. The ETS signal is of shorter duration (200 ps) than the  $\omega_o/2$  signal (700 ps). The half-harmonic signal turns on first and the down-scattering occurs near its peak.

An up-scattering spectrum taken in this same geometry (Fig. 34.10) shows the two peaks associated with ETS. The shorter-wavelength peak, identified with superhot electrons, occurs between  $3\omega_o/2$  and  $2\omega_o$ . The longer-wavelength peak, due to hot electrons, occurs near 400 nm. The latter has been observed regularly, while the former was

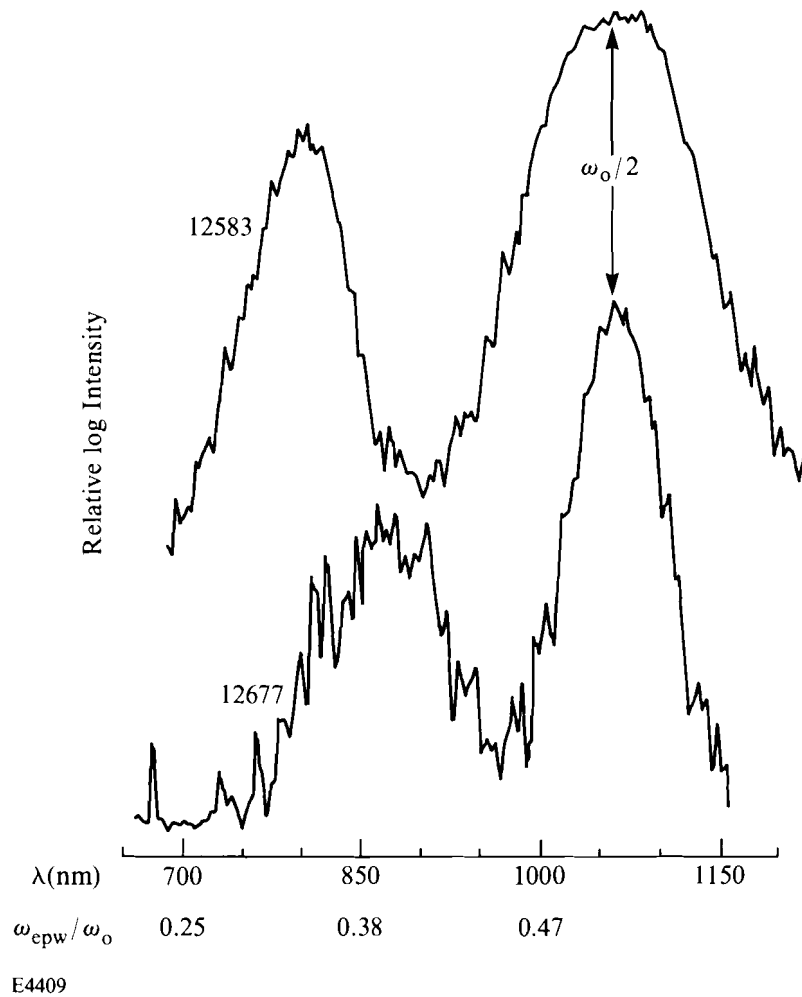


Fig. 34.8  
Down-scattered spectra for the same average incident intensity and measured electron temperature. The variations in the position of the bands are attributed to varying hot spots in the incident laser.

visible only rarely. The absence of this peak is presumably due to the lack of enough superfast electrons.

We present a complete description for one particular shot in Fig. 34.11. This shot had a measured average intensity of  $7 \times 10^{14}$  W/cm<sup>2</sup> and a measured superhot-electron temperature of 17 keV. A better theoretical fit was found using a superhot-electron temperature of 30 keV, which is reasonable considering the uncertainties in the temperature diagnostic. A superhot-electron fraction of 1% was found by comparing the measured down-scatter band with Fig. 34.1. This predicts an up-scatter band between 290 and 350 nm, which corresponds well with the measured peak. Since there was no direct measurement of the hot-electron temperature, we assumed a temperature of 17 keV and fit the second up-scatter peak, at a wavelength longer than 351 nm, with a hot-electron fraction of 1%. This value is below the threshold for down-scattering, which is consistent with our observation of only a single down-scattering band

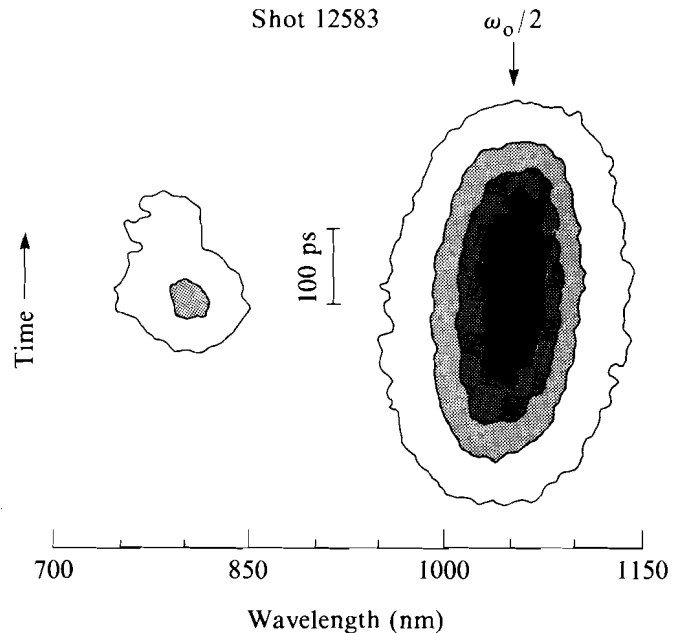


Fig. 34.9  
Typical time evolution of the down-scattering spectra, which begins near the peak of the  $\omega_0/2$  emission and lasts for about 200 ps.

E4410

(from superhot electrons). Therefore, we see that a complete set of data can be explained self-consistently using the ETS theory.

### Discussion

The ETS theory describes the results very well for those shots in which a nearly complete set of experimentally measured parameters could be obtained. However, in other instances one or more of the predicted peaks was missing, especially the shorter-wavelength down-scattering band that we have associated with the hot (but not the superhot) electrons. This may be due to the hot-electron fraction not exceeding the threshold needed for enhanced scattering. At other times, the up-scattering band associated with the superhot electrons was also absent, presumably for similar reasons. The lack of sufficient numbers of hot or superhot electrons may be connected to the lack of hot spots in the laser-beam intensity pattern. Since only a limited amount of energy was at our disposal, the up-scattering ETS threshold could only be surpassed in hot spots of the laser beam where the peak intensity could be many times the average intensity. We infer from our measurements that the random distribution of hot spots, presumably due to air turbulence, is responsible for the infrequent appearance of the short-wavelength up-scatter band.

Two other theories could be advanced to explain the existence of the scattered features we observed. The first is convective stimulated Raman scattering (SRS-C).<sup>9</sup> As discussed previously, this interaction takes place in the plasma corona at densities below quarter-critical. According to this theory, the signature is a scattering band that should

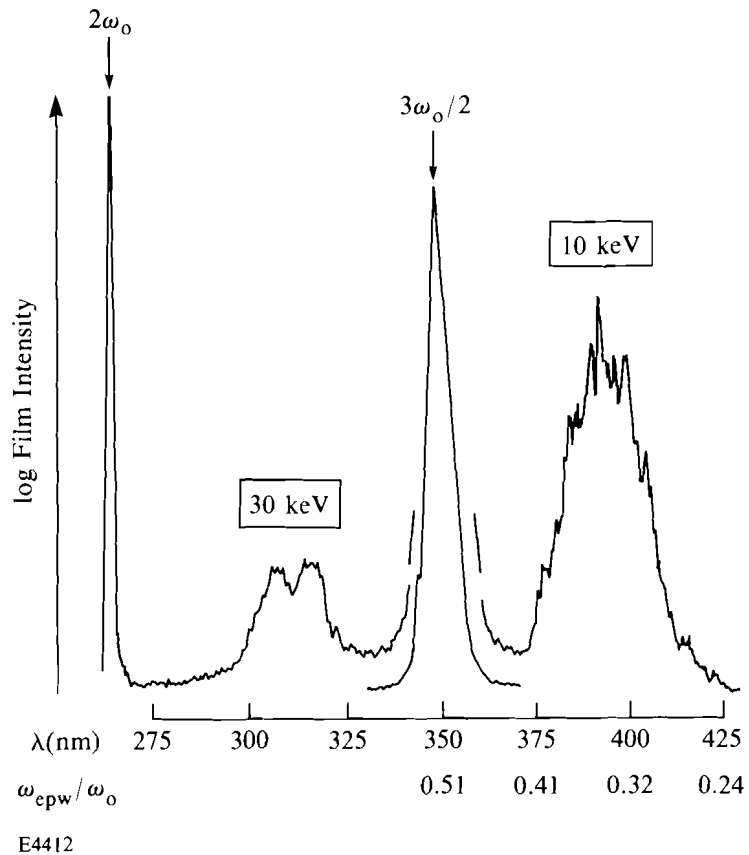


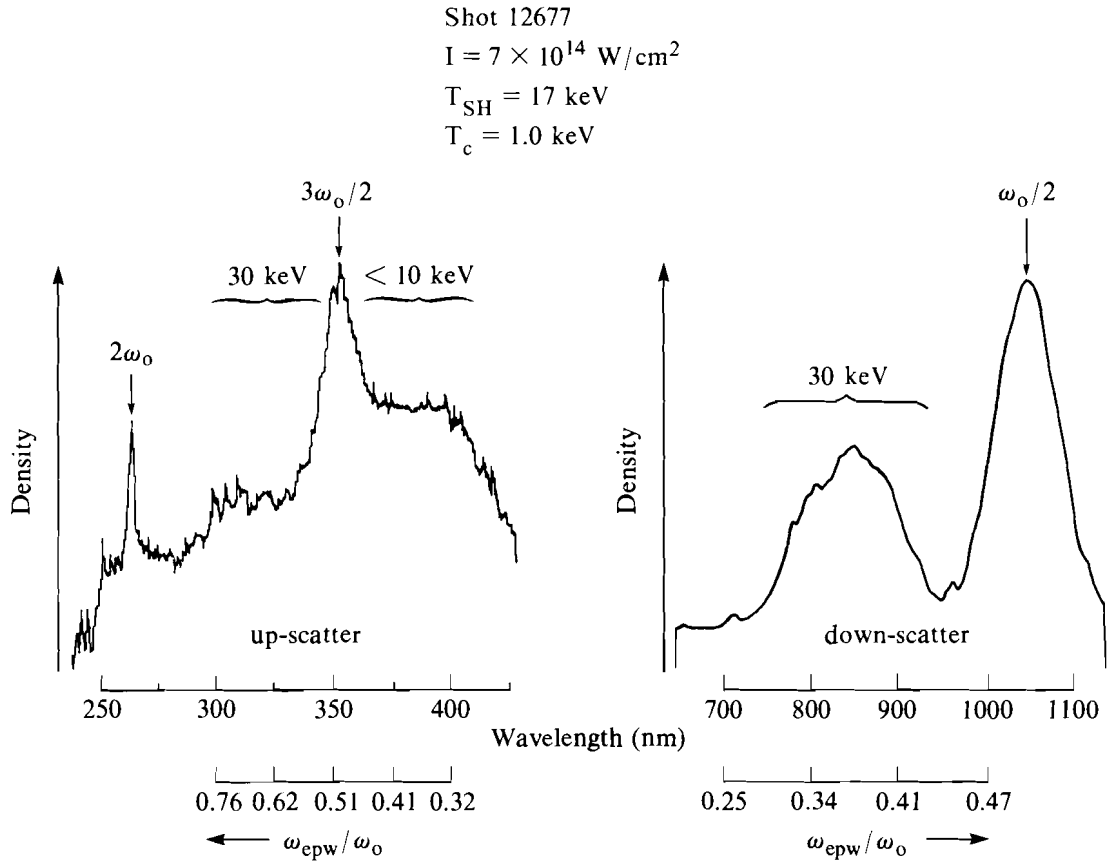
Fig. 34.10

Up-scattering spectrum observed along the density gradient. The two up-scattering features on either side of the  $3\omega_0/2$  peak reflect two electron-temperature components with  $T_h = 10$  keV and  $T_{sh} = 30$  keV.

extend from the half-harmonic of the laser up to a higher frequency, where it is cut off by Landau damping (i.e., near  $k\lambda_D \approx 0.2$ ). Density steepening at the quarter-critical surface must be invoked to explain the gap that appears between the down-scattering band and the  $\omega_0/2$  feature. In addition, the theoretical threshold for SRS-C is usually not exceeded in the intensity region where down-scattering has been seen.<sup>3</sup> In our experiments, this is certainly the case as well.

Stokes mixing has been suggested as an explanation for the existence of both up- and down-scattering bands<sup>6</sup> because the conditions for the SRS instability also allow coupling to a fourth anti-Stokes EM wave at  $\omega_s' = \omega_0 + \omega_{\text{epw}}$ . Normally, the amplitude of this wave is small, since it is nonresonant. At low plasma densities, and for scattering in the forward direction, the degree of off-resonance is reduced and an appreciable level can be reached. Note, however, that the frequency of this wave lies above the laser frequency by the same amount as the down-scattered wave does below it, and cannot exceed  $3\omega_0/2$ . Since the dispersion relation for the up-scattered EM wave will not be satisfied at the density where the instability occurs, some propagation of the plasma wave toward a different density will have to be invoked so that the scattered wave will be observable.

Our observations cannot be explained by Stokes mixing since (a) the scattering bands were not symmetric (see Fig. 34.11, where a scale in terms of  $\omega_{epw}/\omega_0$  has been added for convenience), (b) spectral features above the three-halves harmonic were observed (Figs. 34.5 and 34.10) (a region not accessible to Stokes mixing), and (c) our observations in the backscatter direction are incompatible with the resonant condition for up-scattered light since the plasmon wave vector would be too large.



E4413

Fig. 34.11 Simultaneous up- and down-scattering spectra. The measured electron temperatures for this shot were  $T_c = 1.0$  and  $T_{sh} = 17 \text{ keV}$ . No hot x-ray component was observed for this shot in the x-ray temperature diagnostic, presumably because of insufficient signal emitted by this component relative to the two other temperature components. The incident intensity was  $7 \times 10^{14} \text{ W/cm}^2$  in a 600-ps pulse.

In conclusion, we conducted a series of experiments to observe the scattered-light spectrum from a 527-nm laser-produced plasma. We observed three features: one was down-scattered from the laser frequency and two were up-scattered, one on either side of the three-halves feature. Using several different irradiation and observation geometries, we temporally resolved the down-scattered spectra. In addition, we independently measured the continuum x-ray spectra and determined corresponding electron temperatures. We find good agreement with the ETS model if we assume that the electron temperature distribution can be described by three components: a cold background with  $T_c \approx 1.5 \text{ keV}$ , a hot component created as a by-

product of resonance absorption or the parametric decay instability with  $T_h < 10$  keV, and a superhot component created by the two-plasmon decay instability with  $T_{sh} > 15$  keV. We also find that neither convective stimulated Raman scattering nor Stokes mixing is an adequate explanation of the observed spectra.

#### ACKNOWLEDGMENT

This work was supported by the U. S. Department of Energy Office of Inertial Fusion under agreement No. DE-FC08-85DP40200 and by the Laser Fusion Feasibility Project at the Laboratory for Laser Energetics, which has the following sponsors: Empire State Electric Energy Research Corporation, New York State Energy Research and Development Authority, Ontario Hydro, and the University of Rochester. Such support does not imply endorsement of the content by any of the above parties.

#### REFERENCES

1. LLE Review **19**, 104 (1984).
2. A. Simon and R. W. Short, *Phys. Rev. Lett.* **53**, 1912 (1984).
3. A. Simon, W. Seka, L. M. Goldman, and R. W. Short, *Phys. Fluids* **29**, 1704 (1986).
4. C. L. Shepard *et al.*, *Phys. Fluids* **29**, 583 (1986).
5. R. E. Turner, D. W. Phillion, E. M. Campbell, and K. G. Estabrook, *Phys. Fluids* **26**, 579 (1983).
6. R. E. Turner *et al.*, *Phys. Rev. Lett.* **57**, 1725 (1986).
7. C. S. Liu and P. K. Kaw, in *Advances in Plasma Physics*, Vol. 6, edited by A. Simon and W. B. Thompson (Wiley, New York, 1976), pp. 83–120.
8. W. Seka, E. A. Williams, R. S. Craxton, L. M. Goldman, R. W. Short, and K. Tanaka, *Phys. Fluids* **27**, 2181 (1984).
9. C. S. Liu, in *Advances in Plasma Physics*, Vol. 6, edited by A. Simon and W. B. Thompson (Wiley, New York, 1976), pp. 121–178.
10. R. S. Craxton (private communication).
11. K. Estabrook, W. L. Kruer, and B. F. Lasinski, *Phys. Rev. Lett.* **45**, 1399 (1980).
12. A. B. Langdon, B. F. Lasinski, and W. L. Kruer, *Phys. Rev. Lett.* **43**, 133 (1979).
13. B. Bezzerides, S. J. Gitomer, and D. W. Forslund, *Phys. Rev. Lett.* **44**, 651 (1980).
14. T. Kessler, W. Seka, J. Kelly, D. Smith, R. Bahr, W. Lockman, N. Wong, and J. Soures, *High Power and Solid State Lasers* (SPIE, Bellingham, WA, 1986), Vol. 622, pp. 156–160.
15. P. A. Jaanimagi (private communication).
16. R. L. Keck, L. M. Goldman, M. C. Richardson, W. Seka, and K. Tanaka, *Phys. Fluids* **27**, 2762 (1984).

## 1.B Bounce-Coated Ablation Layers on Fusion Targets

An ablation layer coated on a laser-fusion target must be sufficiently uniform to avoid creating hydrodynamic instabilities during implosion.<sup>1</sup> Any coating method employed should preserve the high degree of sphericity and uniformity obtainable in the starting shell.<sup>2,3</sup> The principal means used to achieve uniform ablation layers on spherical shells has been to bounce the shells on a vibrating surface while they are being coated, so that all sides are identically exposed to the coating process.<sup>4-10</sup> Keeping these very light ( $\sim 10^{-6}$  g) shells from sticking to the surface or to each other during the coating process requires a variety of strategies, including vertical acceleration of the surface sufficient to overcome sticking forces,<sup>4</sup> a plasma to prevent a large surface charge from arising, and others to be discussed.

The low-Z polymer parylene<sup>11</sup> is often used for ablation layers, but is not conventionally applied in the presence of a plasma. Maintaining a low-power plasma sufficient to overcome sticking due to surface charge modifies the parylene coating process considerably, as evidenced by a large increase in coating rate and embrittlement of the coating. This report describes the role of the plasma in the coating process and some of the properties of the coating that result from the use of the plasma.

### Description of Bounce Coating

The physical arrangement of the bounce-coating apparatus is shown in Ref. 5. Parylene monomer enters the coating chamber, prepared as in the conventional parylene process. Argon is also bled in to maintain a pressure of 36 mTorr. A plasma is generated by applying a low-frequency sinusoidal voltage between a flat electrode 5 cm above the shells and the surface on which the shells bounce. Turning on the plasma reduces the monomer pressure (observable on a heated gauge) while increasing the coating rate. The parylene monomer absolute pressure is unknown, but is calculated to be  $\sim 12$  mTorr with the plasma off. This value is determined from the measured coating rate and the known relationship among coating rate, substrate temperature, and monomer pressure.<sup>11</sup> The plasma is maintained at a low power ( $\sim 200$  mW) because a higher power causes particles to form in the vapor. A lower power, on the other hand, is difficult to maintain and results in an increased probability for the lightest shells to stick. To keep out contaminants, shells are inserted and extracted without exposing the coating region to air.

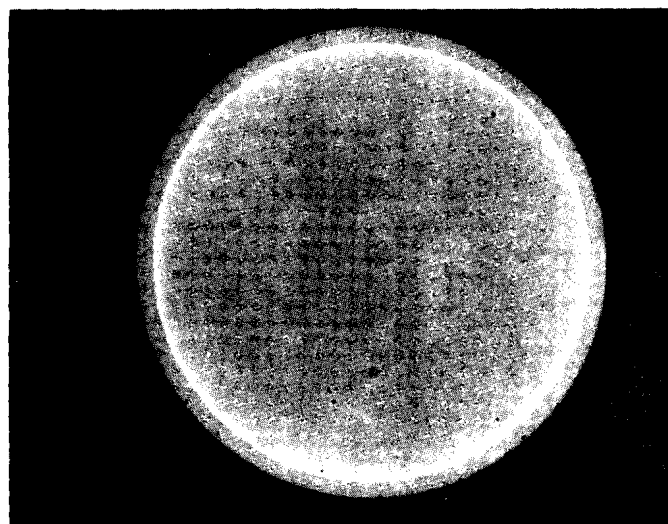
The shells (up to 20 at a time) bounce on the vertically vibrating surface of a mechanical resonator.<sup>4,5</sup> The principal advantage of this resonator over other types of vibrating surfaces is that vertical motion is relatively uniform over the entire surface of area  $20 \text{ cm}^2$ . This uniformity is assured by the nature of the longitudinal mode of vibration used. A constant vibrational amplitude is maintained by a feedback loop. Too high a peak surface velocity can throw shells out of the coating region. To protect against target losses, a thin-foil catcher is glued around the upper edge of the mechanical resonator, increasing its radius by 70%. The foil surface does not vibrate enough

to bounce shells, but a shell accidentally thrown there can be picked up with the probe and returned to the bouncing region. Use of the foil allows use of a peak acceleration of  $5 \times 10^3 \text{ m/s}^2$  at 20 kHz, which is usually sufficient to keep the lightest shells ( $0.3 \times 10^{-6} \text{ g}$ ) bouncing.

A microscope is set up for observing the bouncing shells, allowing the operator to intervene if sticking occurs. Solid glass spheres ( $\sim 240\text{-}\mu\text{m}$  diameter) bounced along with the shells help prevent sticking. If these strategies fail and targets stick, a thin-fiber probe can be manipulated from outside the coating chamber and used to unstick shells without stopping the coating. This method of unsticking is avoided if possible, however, since shells unstuck in this manner after parylene has bonded them to the surface may be left with flaws. Surface flaws can grow as bounce coating proceeds, a process well characterized by others.<sup>7</sup> The preferred way to overcome sticking is to maintain a sufficient vertical acceleration.

The coating thickness is monitored during coating by a reflectometer.<sup>12</sup> The shells, well characterized prior to being coated, are reidentified to the extent possible by diameter measurement and x-ray radiography.<sup>13</sup> A typical radiograph, shown in Fig. 34.12, indicates the high degree of uniformity attained. The best coatings are free of surface features larger than  $\sim 0.2 \mu\text{m}$  in height. The appearance of the surface is slightly smoother than is seen in Ref. 5.

Fig. 34.12  
X-ray radiograph of a bounce-coated  
glass shell.



— 100  $\mu\text{m}$  —

T796

### Role of the Plasma

Maintaining a suitable plasma power during a coating run that lasts several hours requires either automatic control or frequent operator attention. Figure 34.13 shows how the plasma current is measured and controlled. The small plasma current used here ( $\sim 0.3 \text{ mA rms}$ ) is an order of magnitude smaller than the current drawn by capacitive elements of the circuit. In the circuit shown here, the phase of the lock-in amplifier is adjusted so that the output is zero if the plasma is

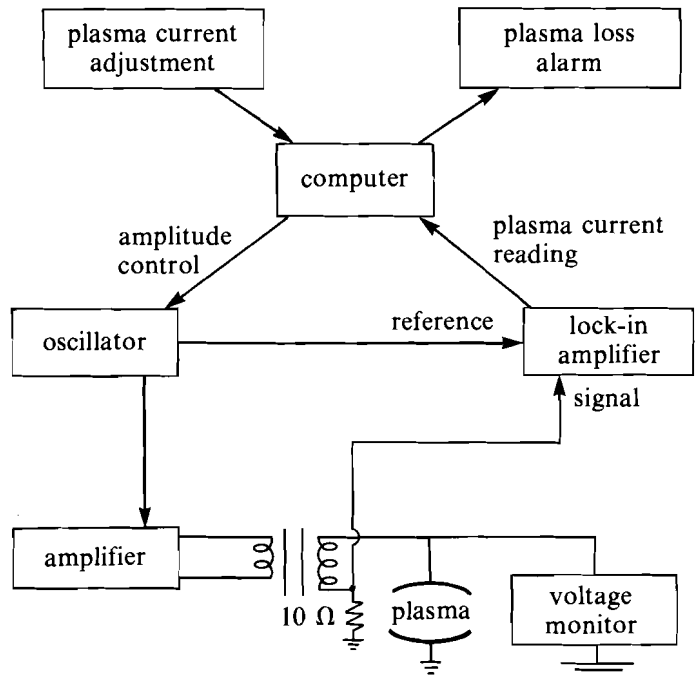
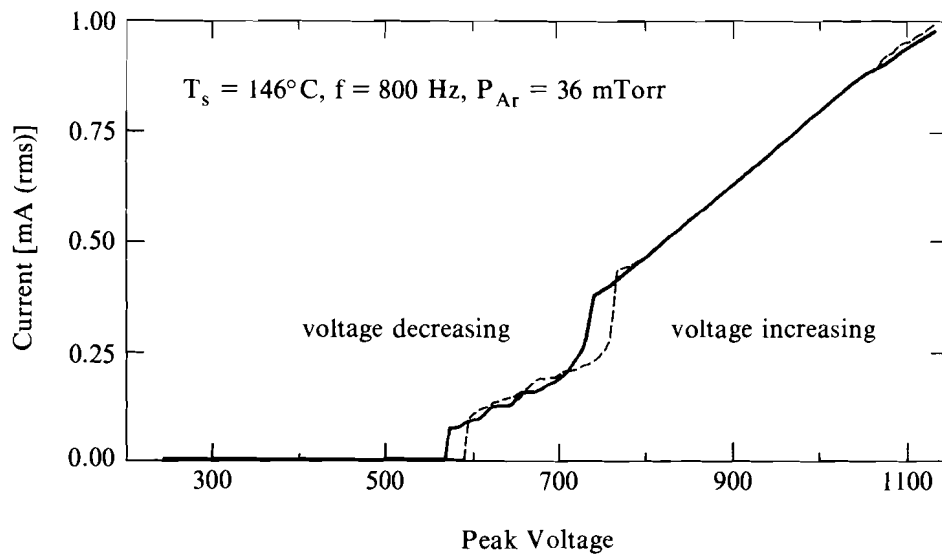


Fig. 34.13  
Circuit for measuring the plasma and closed-loop feedback for maintaining the plasma.

T804

off. This can be done because at low plasma currents, the two currents differ in phase by  $90^\circ$ . (The phase difference is verified by observing that the lock-in amplifier, when its phase is switched by  $90^\circ$ , is insensitive to the plasma being on or off.) The rms plasma current is then the rms voltage read by the lock-in divided by the resistance to ground of  $10\ \Omega$ . At low plasma currents, the current flows only at peak drive voltage, so the plasma power is given by the product of rms plasma current and peak voltage. At the frequency used here, 800 Hz, a low-power plasma is intermittent, consisting of two short current spikes per cycle. When the drive voltage is increased above the values used here, the waveform of the current becomes more complicated and the reading on the lock-in is no longer an accurate measure of plasma current.

The current-voltage characteristic for typical operating conditions of the coating process is shown in Fig. 34.14. The current is an rms value at the drive frequency of 800 Hz. The dimer sublimation temperature  $T_s$  controls the rate at which monomer enters the coating region. The argon pressure  $P_{Ar}$  is measured on a gauge separated from the coating region by a small cold trap that prevents monomer from reaching the gauge. The characteristic curve exhibits two bistable regions, the lower of which is a threshold for the plasma to turn on or off. An operating point just below or within the upper bistable region is commonly used. The bistability causes some difficulty in controlling the plasma, and it is sometimes necessary to tolerate fluctuating values of current as a result. Operating near the lower bistable region risks



T863

Fig. 34.14  
Current-voltage characteristic of parylene-argon plasma showing two bistable regions. The data were taken using a slow sweep of the drive voltage. The bistable regions are not a result of any time constant of the instrumentation.

plasma loss and consequent target sticking. Families of curves like Fig. 34.14 have been taken using various values of  $T_s$  and  $P_{\text{Ar}}$ . There are values of these parameters for which the lower bistable region spans a much wider voltage range, for instance at low values of  $P_{\text{Ar}}$ . Avoiding this wider bistable region is one of the considerations leading to the choice of operating parameters.

The coating rate varies strongly with both plasma power and monomer pressure. It is seen in Fig. 34.15 that starting the plasma more than doubles the coating rate. The coating rate increases rapidly with increasing power, but then begins to level off, suggesting a partial depletion of the supply of incoming monomer. At high coating rates and plasma power, particles of unknown composition form in the coating region. Each curve in Fig. 34.15 has a threshold for particle formation, which is detected visually. Raising the power much above this threshold causes extremely rapid particle formation. Avoiding particle formation is facilitated by finding a chamber and electrode geometry in which the likeliest spot for particle deposition is readily observed and is far away from the targets. The point on Fig. 34.15 usually used for bounce coating is a power of 200 mW and a coating rate of  $2\ \mu\text{m/h}$ , conditions under which no particle formation occurs.

### Bounce-Coated Polymer Shells

Polymer shells bounce coated with parylene are given added strength by the parylene and so can be permeated with gas to a higher internal pressure. For some gases, parylene can also function as a barrier layer that increases the permeation-time constant by a useful amount. It cannot be assumed that the properties of importance here, permeability and tensile strength, are the same for plasma-deposited parylene as for conventional parylene.

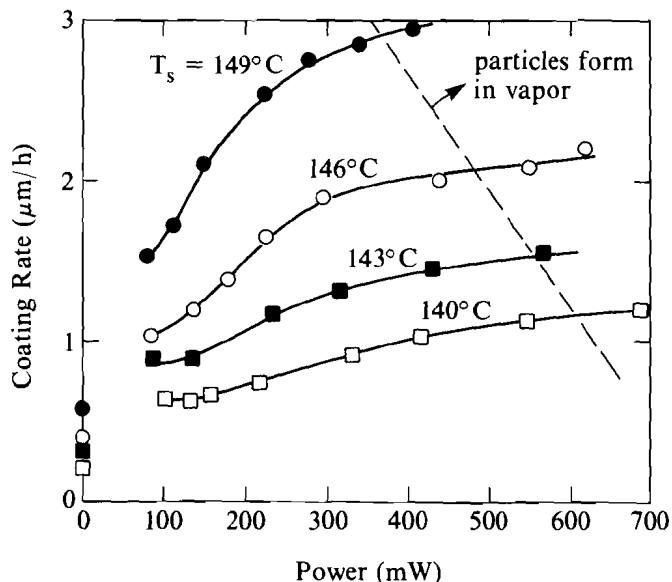


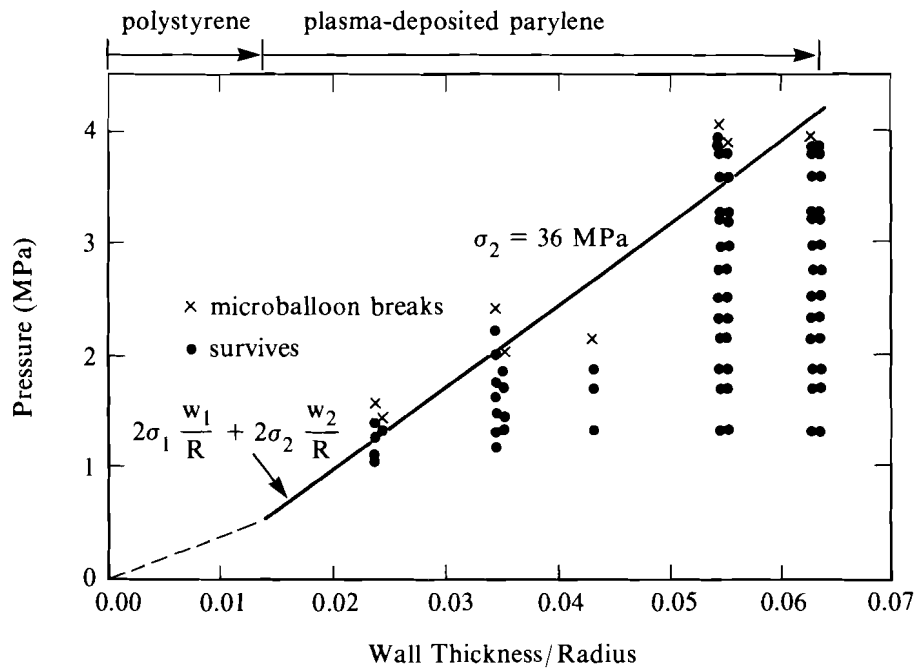
Fig. 34.15  
Variation of coating rate with plasma power and sublimation temperature at  $P_{Ar} = 36$  mTorr. The points at zero plasma power represent the conventional parylene process.

T861

To measure tensile strength, a set of polystyrene shells made at Lawrence Livermore National Laboratory<sup>2</sup> was selected in a narrow range of diameters (472 to 496 μm) and wall thicknesses (3.3 to 3.5 μm, measured with single-direction interferometry). These were bounce coated with five different thicknesses of parylene in the range 2.4 to 12.0 μm. The shells were then permeated with He to various pressures, individually or in small groups, and kept under pressure a long enough time so that the internal pressure would be within 1% of the external pressure. The external pressure was released in 1 to 2 s, a time short enough that no significant internal pressure was lost. Survival or failure of each shell was noted, and the pressure plotted in Fig. 34.16. If the assumption is made that the strengths of polystyrene and parylene may be simply added, the points of highest pressure survival are fitted by

$$P_{max} = 2 \sigma_1 \frac{w_1}{R} + 2 \sigma_2 \frac{w_2}{R} , \quad (1)$$

where the subscript 1 refers to polystyrene and subscript 2 to parylene,  $\sigma$  = tensile strength,  $w$  = wall thickness, and  $R$  = radius. The radii of the two materials are close enough to be treated as equal. Equation (1) may be understood by equating the force trying to push apart two halves of a thin-walled spherical shell,  $\pi R^2 P$ , with the strength of the wall where the hemispheres join,  $2\pi R(w_1 \sigma_1 + w_2 \sigma_2)$ . A least-squares fit of Eq. (1) to the data in Fig. 34.16 yields tensile strengths  $\sigma_2 = 36$  MPa for plasma-deposited parylene and an extrapolated value of  $\sigma_1 = 18$  MPa for polystyrene. The value for plasma-deposited parylene is 80% of the value listed for conventional parylene. The strength for any given shell may be limited by the intrinsic strength of



T864

Fig. 34.16

Survival of polymer shells with internal pressure. The shells are polystyrene bounce coated with various thicknesses of parylene. A fit of the highest-pressure survival data (solid line for the parylene portion, dashed line for polystyrene) to Eq. (1) yields values of the tensile strengths of the materials. The pressure shown is internal minus external pressure.

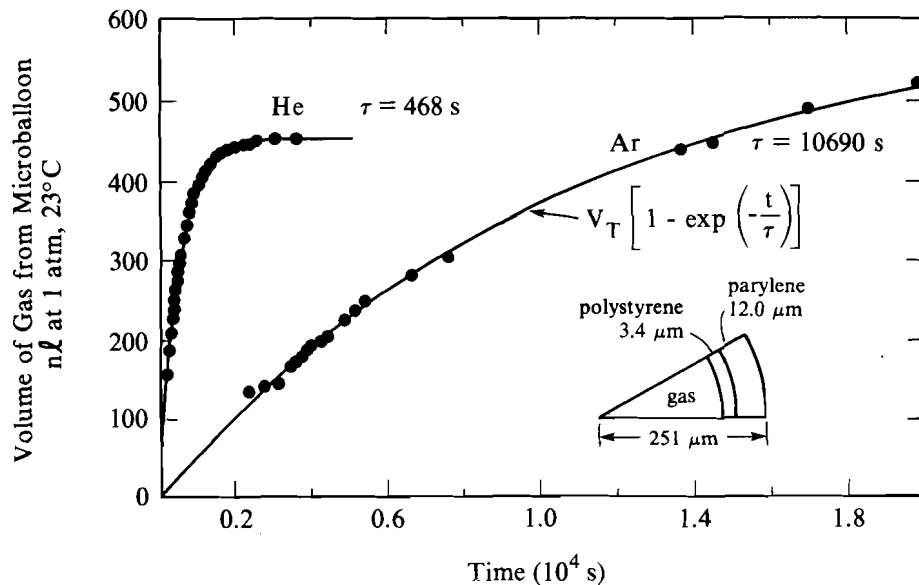
the materials or by a flaw from which a fracture can spread. This may partially account for the scatter in the data.

The tensile strength measurements required knowledge of lower and upper limits for the permeability of plasma-deposited parylene to He gas. To obtain values of permeability, several shells that had already survived permeation to moderate or high pressures were permeated again with He or Ar, and their outpermeation was measured as a function of time. The measurement was based on a method described by E. Lilley,<sup>2,14</sup> in which a shell is placed in the closed end of a glass capillary tube and permeated with a gas. Just after removal from the permeator, a small amount of Hg is injected into the open end of the capillary, sealing the capillary, but leaving the Hg free to move as gas permeates out of the shell. The prepared capillary is then placed inside a sealed glass tube much larger in volume, so that atmospheric pressure variations do not affect the Hg position. By monitoring the position of the Hg, the volume of gas permeating out of the shell is measured as a function of time.

The permeation measurements for one shell are shown in Fig. 34.17. If the pressure inside the shell decreases with time as  $\exp(-t/\tau)$ , where  $\tau$  is the time constant to be determined, then the volume of gas diffusing from a shell is

$$V(t) = V_T [1 - \exp(-t/\tau)], \tag{2}$$

where  $V_T$  is the total volume of gas from  $t = 0$  to time  $t \gg \tau$ . The



T865

Fig. 34.17

Two permeation tests of a bounce-coated polymer shell with dimensions indicated. The solid lines are fits of the data to Eq. (2). Different permeation pressures were used for the two gases. Values of permeability of plasma-deposited parylene are obtained from the values of  $\tau$ .

position of the Hg at time  $t$ ,  $x(t)$ , can be expressed

$$x(t) = x_0 + V(t)/A, \tag{3}$$

where  $x_0$  is the position at  $t = 0$  and  $A$  is the cross-sectional area of the capillary. Combining Eqs. (2) and (3), the resulting equation for  $x(t)$  is fit by least squares to the measured data. The three fitting parameters are  $x_0$ ,  $V_T$ , and  $\tau$ . To plot the data in Fig. 34.17, the  $x(t)$  data points were converted to  $V(t)$  using Eq. (3) and the value of  $x_0$  obtained from the fit. The data are fit well by Eqs. (2) and (3).

The measured values of  $\tau$  imply permeabilities of plasma-deposited parylene for He of  $7.8 \times 10^{-16}$  mol/m s Pa and for Ar of  $3.3 \times 10^{-17}$  mol/m s Pa, both at room temperature. (The permeability of polystyrene, an order of magnitude higher for both gases, was taken into account.) The value for He is 7% lower than the value listed for conventional parylene.<sup>15</sup> A value for Ar is not listed. The permeability to Ar is low enough that a shell containing Ar may be removed from the permeator and either used immediately as a target, or else coated with a metal barrier layer while still containing a significant (and predictable) portion of the original pressure. Some targets made by the latter method have been irradiated by the OMEGA laser.

### Conclusion

The continuing development of parylene bounce coating has been described, and some of the constraints on process parameters given. The quality and reliability achieved in this process has allowed hundreds of targets to be coated with parylene ablation layers and irradiated by the OMEGA laser. The substantial tensile strength

achieved with bounce-coated parylene layers has useful implications for the design of polymer shell targets. As a permeation barrier, parylene is useful only for gases as large in atomic radius as Ar. When used with another material as a barrier layer, however, such as polyvinyl alcohol or Al, a layer of bounce-coated parylene can provide the necessary strength for holding high internal pressures of D<sub>2</sub> or DT.

#### ACKNOWLEDGMENT

This work was supported by the U. S. Department of Energy Office of Inertial Fusion under agreement No. DE-FC08-85DP40200 and by the Laser Fusion Feasibility Project at the Laboratory for Laser Energetics, which has the following sponsors: Empire State Electric Energy Research Corporation, New York State Energy Research and Development Authority, Ontario Hydro, and the University of Rochester. Such support does not imply endorsement of the content by any of the above parties.

#### REFERENCES

1. R. L. McCrory, L. Montierth, R. L. Morse, and C. P. Verdon, in *Laser Interaction and Related Phenomena, Vol. 5*, edited by H. J. Schwartz, H. Hora, M. Lubin, and B. Yaakobi (Plenum, New York, 1981), pp. 713-742.
2. A. K. Burnham, J. Z. Grens, and E. M. Lilley, *J. Vac. Sci. Technol. A* **5**, 3417 (1987).
3. KMS Fusion Inc., Annual Technical Report, 1981.
4. S. M. Gracewski and R. Q. Gram, *J. Vac. Sci. Technol. A* **5**, 2941 (1987).
5. R. Q. Gram, H. Kim, J. F. Mason, and M. Wittman, *J. Vac. Sci. Technol. A* **4**, 1145 (1986).
6. W. L. Johnson *et al.*, *Amer. Chem. Soc. Div. Polym. Chem.* **19**, 544 (1978).
7. S. A. Letts, D. W. Myers, and L. A. Witt, *J. Vac. Sci. Technol.* **19**, 739 (1981).
8. R. Liepins *et al.*, *J. Vac. Sci. Technol.* **18**, 1218 (1981).
9. S. F. Meyer, *J. Vac. Sci. Technol.* **18**, 1198 (1981).
10. W. L. Johnson *et al.*, in *Plasma Polymerization*, edited by M. Shen and A. T. Bell, Vol. 108 of American Chemical Society Symposium Series (American Chemical Society, 1979), p. 315.
11. Union Carbide, parylene technology brochure.
12. H. Kim, T. Powers, and J. Mason, *J. Vac. Sci. Technol.* **21**, 900 (1982).
13. H. Kim and M. D. Wittman, *J. Vac. Sci. Technol. A* **3**, 1262 (1985).
14. E. Lilley, technical memorandum, Lawrence Livermore National Laboratory (unpublished).
15. M. A. Spivack, *Rev. Sci. Instrum.* **41**, 1614 (1970).

## **Section 2**

# **ADVANCED TECHNOLOGY DEVELOPMENTS**

### **2.A Optical Probes for the Characterization of Surface Breakdown**

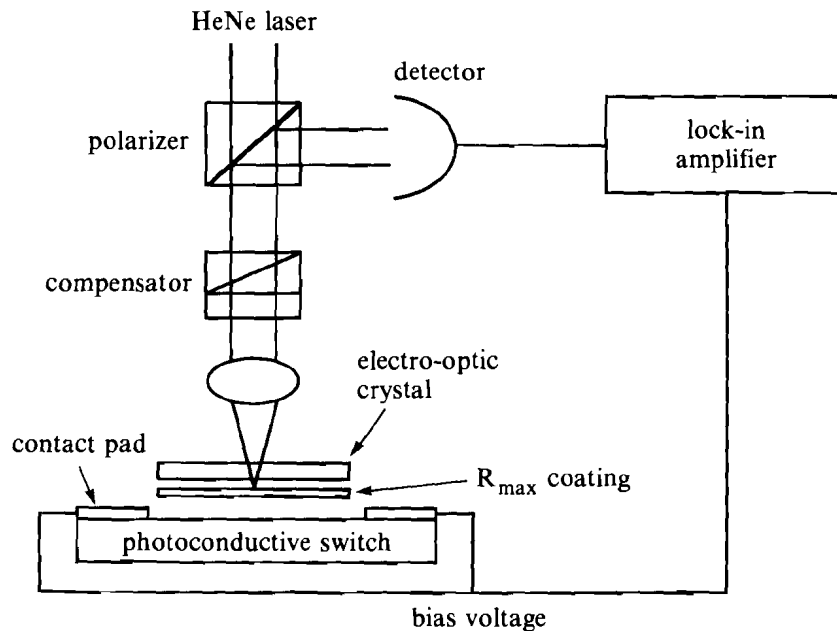
The driving force behind this investigation is the need to understand surface breakdown on semiconductors. Many applications require that electrodes on semiconductor materials be placed in geometries where significant electric fields are developed across their surfaces. This generalization is true over a wide range of applications. High-speed semiconductor circuits, such as those in very large scale integration (VLSI) applications, place relatively small voltages across the electrodes, but the electrode separation is made as small as possible to reduce the signal propagation time through the device. This results in large electric fields. Pulsed-power semiconductor switches have relatively large electrode separations, but they are required to hold off very large voltages. Surface breakdown is the major limiting factor in the operation of these elements. Whether the circuits are for high-speed logic or pulse power, the need to keep the surface electric fields below the level where surface breakdown will occur places a minimum-size restriction on the devices that can be constructed. Despite its relevance, the mechanism of surface breakdown on most materials is poorly understood. Semiconductors in particular are difficult to understand because of the presence of free carriers on the surface that modify the distribution of the electric field. This report presents the development of an imaging technique to monitor the temporal evolution of surface electric fields. These experiments seek to use this information to reconstruct the dynamics of the charge carriers on the semiconductor surface.

The electro-optic, or Pockels, effect is a novel probe of surface electric fields.<sup>1</sup> It can modulate an optical probe to produce an optical replica of the electric field under investigation. The unique features of electro-optic sampling are its speed and noninvasive nature. The response time of the electro-optic material is of the order of femtoseconds, which allows for extremely high bandwidth signal acquisition. In addition, electro-optic sampling techniques have measured electrical rise times as short as 300 fs without loading the circuit.<sup>2</sup> Because the probe is optical, no electrical contacts, which can perturb the device under test, are needed. The optical coupling also means that the detection electronics are isolated from any dangerous high-voltage transients at the test circuit.

**Electro-Optic Probing**

An electro-optic crystal placed in the fringing electric field above the semiconductor surface experiences a change in its birefringence as a function of the electric field. The change in the birefringence is monitored by probing the crystal with polarized light, as shown in Fig. 34.18. The light passes through a polarizer; a waveplate, to provide an adjustable bias to the transmission; the electro-optic crystal; and then reflects off a dielectric mirror to retrace its path. Because of the waveplate, the polarizer is effectively crossed with respect to itself. The Pockels effect can be viewed as the mixing of a dc electric field and an optical field in a crystal to produce a new optical field with its polarization rotated with respect to the original optical field. When the

Fig. 34.18  
Surface field tester for photoconductive switches.



Z265

crystal is placed between crossed polarizers, the transmission is given by

$$T = \sin^2\{(K E d\chi) + \phi\}/2, \quad (1)$$

where  $E$  is the magnitude of the dc electric field,  $d\chi$  is the optical path length through the crystal,  $\phi$  is a constant optical rotation due to the waveplate and static birefringence of the crystal, and  $K$  is a constant that depends on material parameters, the crystal orientation, and the frequency of the optical field.<sup>3</sup> By choosing the type of crystal and its orientation, the Pockels effect can be made sensitive to only one spatial component of the applied electric field.

The dielectric mirror is bonded directly to the electro-optic crystal and the entire assembly is placed directly on top of the surface to be monitored, which has two rectangular electrodes separated by a fixed distance. The crystal used in these experiments was LiTaO<sub>3</sub>. Its optic axis was perpendicular to both the direction of light propagation and the edges of the electrodes. Thus, the optic axis was oriented along the electric field lines, and the Pockels effect was sensitive to only the component of the electric field along that axis.

### Detection Systems

The principal assumption of this work is that the measured electric field will not be uniform over the surface being measured. Two configurations have been used to detect the spatial and temporal variations of the electric field. The initial measurements investigated the low-voltage, quasi-static configuration of the surface electric field. A piece of LiTaO<sub>3</sub> was placed across evaporated metal contacts on both silicon and gallium arsenide. A time-varying potential was induced across the contacts, causing a modulation of the birefringence of the LiTaO<sub>3</sub> in both space and time via the Pockels effect. A tightly focused cw HeNe laser, with a spot size of approximately 40  $\mu\text{m}$ , probed the change in birefringence, as illustrated in Fig. 34.18. The spatial profile was obtained by translating the electro-optic crystal and semiconductor so that different points were illuminated by the laser beam. The low voltage applied to these devices produced very weak modulation of the optical signal, requiring that the signal be extracted with phase-sensitive detection. This experiment demonstrated that we could spatially resolve the surface electric field on the surface of the semiconductor.

The data acquired as described above had two serious drawbacks. It lacked temporal resolution, and required that the beam be scanned spatially to acquire the total spatial variation of the field. Such conditions are incompatible with the need to record spatially nonlocal, transient events typical of a surface breakdown. The second phase of our investigation addressed these issues.

Short-pulse laser probes improve the time resolution. A single light pulse from a frequency-doubled, mode-locked, amplified Nd:YAG laser samples the electric field only while it traverses the sampling crystal (approximately 100 ps). This technique works with a single

optical pulse only at field strengths that are comparable with the field necessary to cause the direction of the polarization vector in the sampling crystal to change by one-half wave (approximately 1–10 kV/mm). Otherwise, the optical modulation would be too weak to be extracted without the aid of extensive signal processing. The study of surface breakdown events, where the sample may be damaged on a single shot, requires unambiguous detection in a single shot. With short-pulse lasers, it is possible to take 100-ps snapshots of any given event. A series of snapshots of the surface electric field can be taken to record the temporal variation in the field.

The spatial variation in the surface field can be monitored by illuminating the entire area of interest. Instead of using a single detector and scanning a tightly focused spot, a detector array captures an image of the entire field of interest. Each detector element measures only a small portion of the electric field. This experiment has been carried out using an 512-element, linear intensified diode array. A 2-mm gap with identically prepared gold-coated, laser-annealed contacts on intrinsic silicon (7000  $\Omega$  cm) was pulse biased with a short electrical pulse synchronized with the laser pulse. A 50- $\Omega$  load was placed on the low side of the silicon and the leakage through the material was monitored. The lack of photoconductive switching at the load guaranteed that none of the light coupled through the dielectric mirror into the silicon; it is important that light does not perturb the field. During the actual acquisition of data, the load was attached directly to the ground. The laser illuminated a circular region on the silicon surface, and the detector acquired a one-dimensional slice of the electric field on a line joining the two electrodes midway between the ends of the electrodes. This is the first demonstration of imaging technology applied to electro-optic field measurements.

### Surface Field Distribution

The electric field distribution produced by the electrode distribution used in these experiments is not uniform. It is a common field configuration encountered when fabricating devices on wafers (e.g., coplanar transmission lines between transistors in VLSI circuits or photoconductive switches fabricated on wafer substrates). The field lines in a plane perpendicular to the surface are shown in Fig. 34.19(b). They may be derived from the simple case illustrated in Fig. 34.19(a) by the operation of the conformal transformation<sup>4</sup>

$$z = 2 \ln \left\{ [1 + \sin(w)]^{1/2} + [b_z + \sin(w)]^{1/2} / (b_z - 1)^{1/2} \right\}, \quad (2)$$

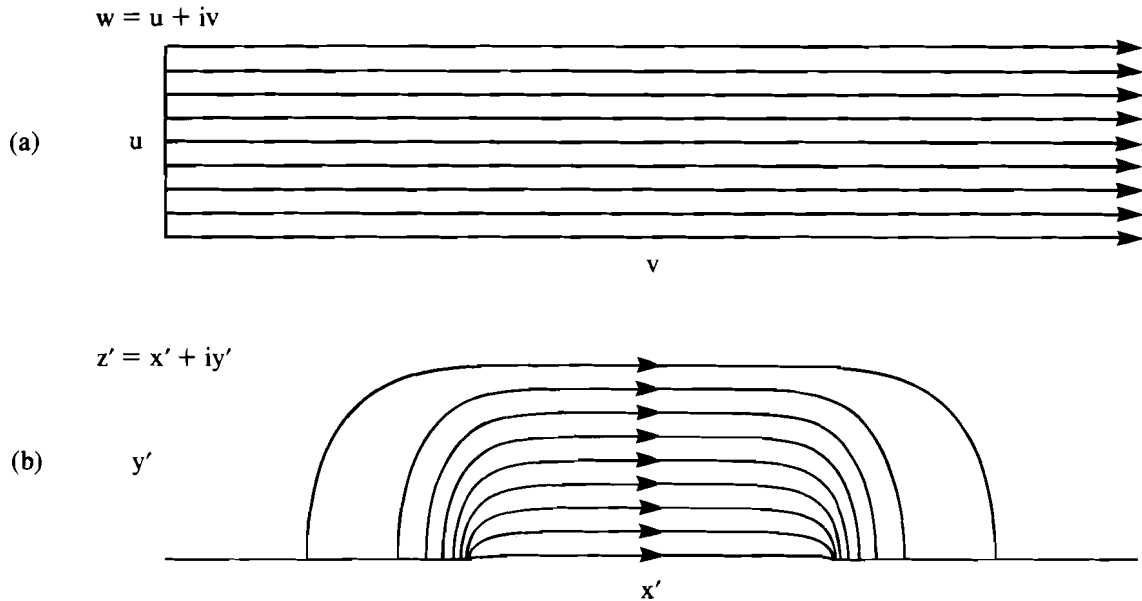
followed by the second transformation

$$z' = w_d - 2 \ln \left\{ \frac{[1 + \sin(iz + \frac{\pi}{2} - iw_g)]^{1/2} + [b_z + \sin(iz + \frac{\pi}{2} - iw_g)]^{1/2}}{(b_z - 1)^{1/2}} \right\}, \quad (3)$$

where

$$b_z = 2 \coth^2 (\pi \ell_c / 2 \ell_s) - 1 \cong 1 \quad (4)$$

$w_g$  is the normalized gap width,  $\ell_c$  is the electrode length,  $\ell_s$  is the substrate thickness,  $w = u + iv$ , and  $z = x + iy$ .



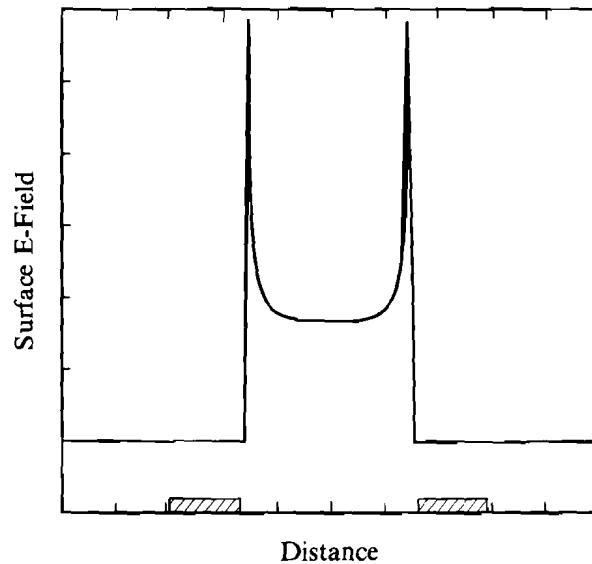
Z434

Fig. 34.19  
Conformal mapping of parallel to coplanar electrodes.

These transformations fold the electrode end faces out into the coplanar geometry. The second transformation is only valid if the transformed plane is at infinite distance from the first plane because the electric field lines must be normal to the second plane. However, if the electrodes are sufficiently far apart, the deviation from normal incidence is negligible. These transformations define the expected value of the electric field throughout the volume of the semiconductor, provided that the measurement is not taken near the corners of the electrodes. The fringing field outside of the semiconductor can be inferred from electromagnetic theory (i.e., the tangential component of the electric field is continuous across a dielectric interface).

From the known electric field configurations in Fig. 34.19(a), the electric field in Fig. 34.19(b) can be calculated. For the type of electro-optic crystal that was used in this experiment, the electric field along the  $x'$  axis in Fig. 34.19(b) was measured. Figure 34.20 shows the field in the plane of the interface; the features are exactly as expected. Above the contacts the electric field is normal to the surface. Therefore, the field along the  $x'$  axis is zero. At the edge of the contacts the field lines bunch up due to the attraction of charges on the opposing electrodes. This is not what is actually measured, however; what is actually measured is the phase shift

$$\theta = \int_{IA} dA \int_0^L KE_{x'}(x, y) dx . \tag{5}$$



Z470

Fig. 34.20  
Surface electric field.

This integral is over the illuminated area ( $IA$ ) and the thickness of the electro-optic crystal ( $L$ ) and is clearly dependent on that thickness. Figure 34.21 shows the integrated detected signal as a function of the electro-optic crystal thickness. The uppermost curve indicates what happens if the crystal is so thick that the integral extends over all the field lines. The surface features are completely obscured because the total integrated flux is conserved between the electrodes. Alternatively, if the crystal is too thin, then the modulation imparted to the light signal becomes very small. The amount of rotation is proportional to the optical path length in the crystal. An intermediate thickness ( $\sim 1/4$  to  $1/5$  of the distance between the electrodes) must be chosen that balances the magnitude of the extracted signal with the smearing due to the path-length integration. Additional smearing of the detected signal is also incorporated into the calculation of the curves in Fig. 34.21. The signal must be averaged over either the laser spot size or the size of the detector element on which it is imaged. In Eq. (5), this is represented by the integral over the illuminated area.

### Results

The usefulness of this technique has been demonstrated at low voltage, where the preparation of the contacts on the semiconductor has been shown to influence the dc electric field distribution. This is the work that was done with the cw probe and the phase-sensitive detection. The primary purpose of the cw experiments was to demonstrate that we could detect spatial variations in the field. The electric field was essentially dc (actually a low-frequency, 1-kHz, square wave). In addition to demonstrating the ability to monitor surface fields, these measurements proved a reliable method of characterizing the contacts. Figure 34.22 shows a cross-sectional view

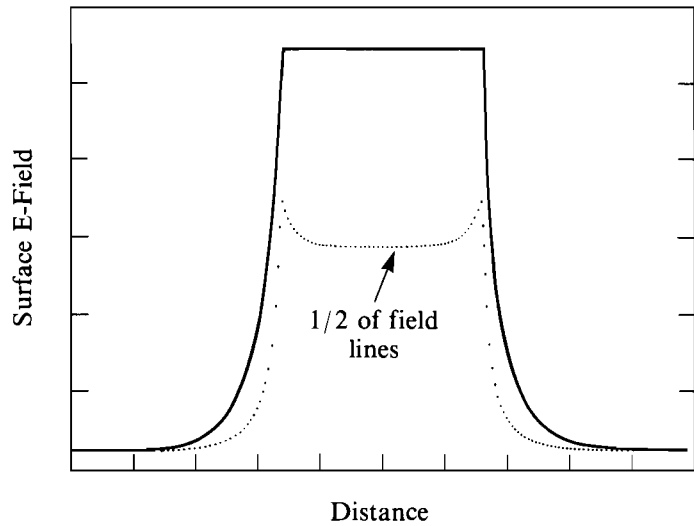


Fig. 34.21  
Integrated surface electric field profile—1/2  
of field lines.

Z428

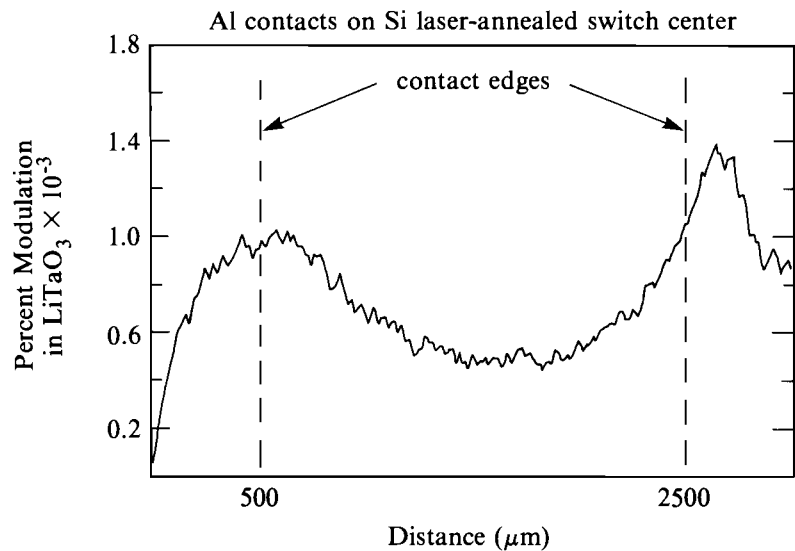


Fig. 34.22  
Surface field profile.

Z283

of the field along the center line between the contact pad on silicon. The figure shows the general features that are expected: the bunching at the contacts and the tailing off at the electrodes. The sampling crystal was thick with respect to the electrode separation. Therefore, the peaks exhibit a significant amount of smearing. What is most interesting is the asymmetry of the electric field. Because the contacts were identically prepared, no asymmetry was expected from the material properties of the sample. When the polarity of the applied

bias was reversed, the asymmetric field distribution also reversed. This indicated that the contacts were not ohmic with respect to the different carrier species (electrons and holes).

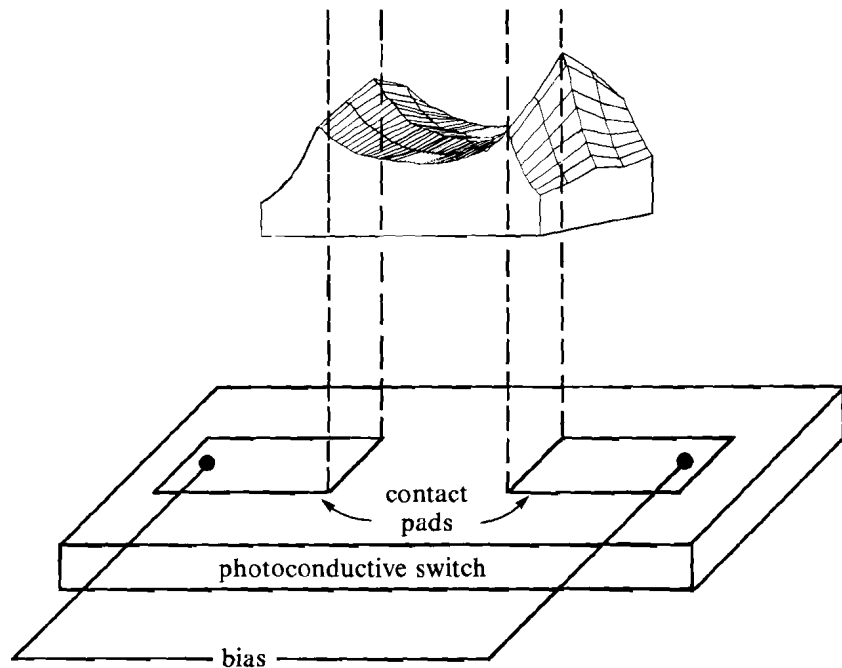
The cw data also showed that a full two-dimensional map of the electric field could be acquired. Figure 34.23 is an axonometric plot of the electro-optic image of the electric field on a silicon switch. The electric field tails off as the probe moves away from the center line of the electrodes.

The time-resolved data was taken to determine the time scale on which the asymmetry illustrated in the cw data evolved. The data was taken by grounding one of the electrodes on a sample prepared on high-resistivity silicon ( $\rho = 7 \text{ k}\Omega \text{ cm} = 70 \text{ }\Omega\text{m}$ ). The dielectric relaxation time of this material is given by the product

$$\rho\epsilon = (70 \text{ }\Omega\text{m} \times 11.9 \times 8.85 \times 10^{-12} \text{ F/m}),$$

where  $\epsilon$  is the dielectric constant of the silicon. Thus, on time scales less than 7 ns, silicon will have a transient response to an applied electric field. A photoconductive switch was used to pulse bias the test structure on a time scale less than 200 ps. One electrode was grounded and the other was attached to a terminated 50- $\Omega$  line driven by a photoconductive switch. The switch was triggered with a 1.06- $\mu\text{m}$  light pulse from a Nd:YAG regenerative amplifier. A 0.532- $\mu\text{m}$  pulse, derived by frequency doubling a portion of the 1.06- $\mu\text{m}$  light, probed the LiTaO<sub>3</sub> crystal. An optical delay line in the path of the 1.06- $\mu\text{m}$  light provided a variable time delay in between the voltage and probe.

Fig. 34.23  
Surface field and contact arrangement.



Z267

The optical image of the electric field was measured with a gated diode array at various time delays between the pump and probe. Figure 34.24 shows three traces of the surface electric field of a device with a 2-mm gap pulsed with 1 kV at various time delays. The units of vertical axis are in percent modulation of the light signal. This is the signal obtained with the voltage on, minus the signal with the voltage off, divided by the signal with the voltage off. Thus, the detected modulation was relatively immune to variations in the illumination profile. At very early times [curve (a)], very little voltage has built up but the device appears to be symmetric in response to the electric field. Curve (b), 166 ps later, shows that a significant voltage has built up across the device and the field is still symmetric. At 332 ps after (a), curve (c) shows that the voltage is still rising but the field displays a definite asymmetry.

The simple explanation of these data is that at early times the electrical inertia of the silicon prevents it from reacting to the field. The device then behaves as if it were a perfect dielectric. The field rises symmetrically on both electrodes and is determined only by the

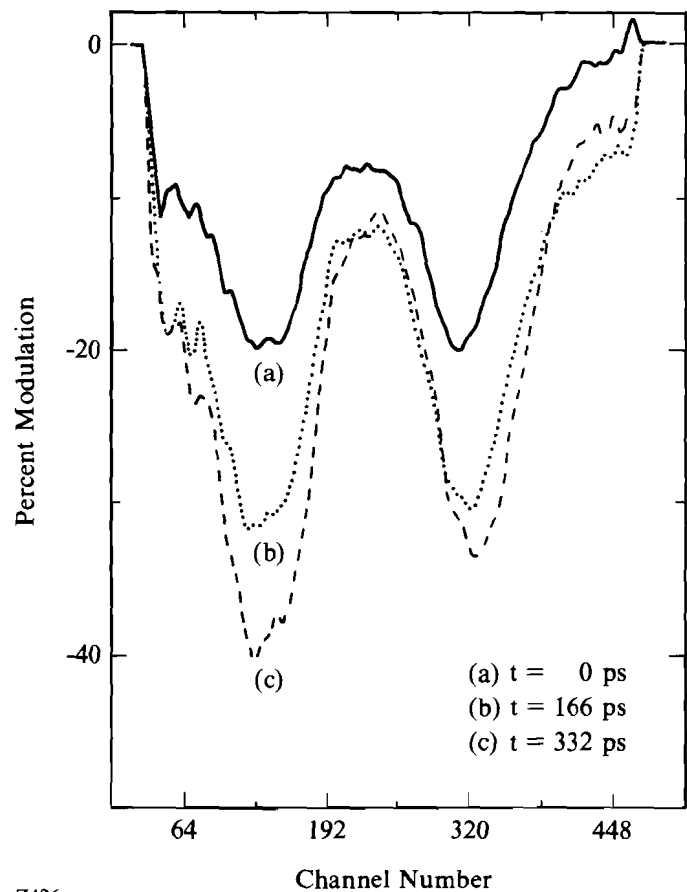


Fig. 34.24  
Surface electric field on silicon versus time.

electrode configuration. Later, as the charge carriers in the silicon begin to rearrange in response to the field, the field itself is modified by the charges in the silicon. Thus, the asymmetry seen in the cw data begins to manifest itself on the time scale of a few hundred picoseconds. This shows that it is possible to probe the transient response of a semiconductor that has been biased on a time scale that is short compared to the dielectric response time of the material.

### Conclusion

At applied fields less than those necessary to cause breakdown, information about the semiconductor device could be readily obtained from the electro-optic imaging data. In the dc biasing case, the contacts were asymmetric with respect to the applied voltage. One contact always had a higher field enhancement at the edge than the other. The enhancement shifted as the polarity of the applied voltage reversed. Such field enhancements are probably due to differences in the injection of holes and electrons at the contacts, and may play an important part in initiating breakdown. The pulse bias case illustrated that this data could be taken on a very short time scale and that transient structure of the electric field can be observed. Although the data shown were averaged over several shots, the 40% modulation can easily be seen in a single shot. By probing at different times and places, we can produce a two-dimensional map of the time evolution of the electric field on a semiconductor surface. Future work will investigate surface breakdown. The electric field will be pulse biased at or near the surface flashover point. The interactions between the electric field and the free carriers can be monitored during a breakdown event. The temporal map of the semiconductor surface field will be taken as described above, with a delay between the pump and probe pulses. An additional feature must be added to the experiment, however. Immediately after the device has been probed with the green pulse, an infrared light pulse will illuminate the device and drive it into the photoconducting state. This will collapse the field and prevent the surface from being destroyed by a surface arc before the full temporal map can be accumulated.

### ACKNOWLEDGMENT

This work was supported by the Laser Fusion Feasibility Project at the Laboratory for Laser Energetics, which has the following sponsors: Empire State Electric Energy Research Corporation, New York State Energy Research and Development Authority, Ontario Hydro, and the University of Rochester. Additional support was provided by SDIO/IST and managed by ONR under contract No. N00014-86-K-0538. Such support does not imply endorsement of the content by any of the above parties.

### REFERENCES

1. K. E. Meyer and G. Mourou, in *Picosecond Electronics and Optoelectronics*, edited by G. A. Mourou, D. M. Bloom, and C. H. Lee (Springer-Verlag, Berlin, 1985), pp. 46-49.
2. J. A. Valdmanis, G. A. Mourou, and G. W. Gabel, *Appl. Phys. Lett.* **41**, 211 (1982).
3. A. Yariv, *Quantum Electronics*, 2nd ed. (John Wiley & Sons, New York, 1975), p. 340.
4. P. M. Hall, *Thin Solid Films* **1**, 277 (1967).

## 2.B Regenerative Amplification in Alexandrite of Pulses from Specialized Oscillators

In a variety of laser sources capable of reaching high energy levels, the pulse generation and the pulse amplification are physically divided among two or more subsystems. An oscillator generates a low-energy seed pulse with the appropriate temporal and spectral features; then, an amplifier stage increases the seed pulse to the desired energy level. When large gains are desired, numerous amplification stages may be required.

Regenerative amplification is an attractive way of limiting the size of the amplifier chain. A seed pulse is injected into a laser resonator that contains a gain medium. The pulse is amplified over many passes through the medium until the gain reaches saturation, and the pulse is then switched out of the resonator cavity. Ideally, the pulse's spectral and temporal characteristics are determined by the oscillator, while the energy output is a function of the regenerative amplifier alone. This technique has been applied to numerous laser media, either flash pumped<sup>1-3</sup> or cw pumped,<sup>4,5</sup> over the last decade. This article describes the use of an alexandrite flash-pumped regenerative amplifier to increase the energy of the output from various specialized oscillators.

### Regenerative Amplifier

Alexandrite is a solid-state lasing medium with an output wavelength that can be continuously tuned over 700–810 nm.<sup>6</sup> Due to its very broad pump bands, long fluorescent lifetime (250  $\mu$ s at 300°K), high saturation fluence (20 J/cm<sup>2</sup>),<sup>7</sup> and low stimulated emission cross section ( $7 \times 10^{-21}$  cm<sup>2</sup> at 300°K), alexandrite can store large energy densities efficiently. In addition, with its large lasing bandwidth it should be capable of amplifying pulses as short as 8 fs. Another favorable property of alexandrite is its low refractive index dispersion near the center of the lasing band.<sup>8</sup> However, because of the low stimulated emission cross section, it is difficult to obtain high gain. Single-pass gain of a typical alexandrite amplifier is between 2.0–6.0. In order to have a large overall gain, many passes through the active alexandrite medium are necessary. Regenerative amplification is one of the most elegant multipass configurations. This technique was first used to amplify low-energy mode-locked pulses in Nd-doped materials.<sup>1,9</sup>

Our regenerative amplifier consists of two high reflectors, the laser medium, a thin-film polarizer, a static quarter-wave plate, and a Pockels cell. For wavelength tunability off gain center, the alexandrite regenerative amplifier also incorporates a birefringent tuner or a pellicle. The 1.5-m-long resonator has a large TEM<sub>00</sub> mode with a beam radius  $w_0$  of approximately 0.5 mm. The amplifier could be operated at repetition rates as high as 30 Hz.

A single Pockels cell controls the injection of the seed pulse and the cavity dumping after amplification. The Pockels cell driver is

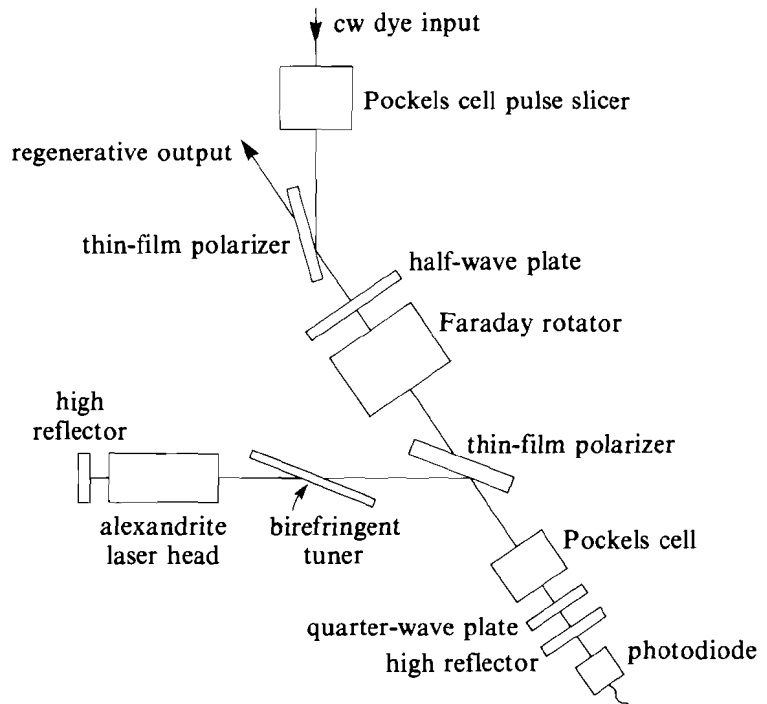
described elsewhere.<sup>10</sup> The intracavity polarizer has a broadband coating (50 nm) and can be used in either transmission or reflection. For some experiments the static quarter-wave plate was found to produce a strong etalon effect. To overcome this, the Pockels cell alignment was adjusted to provide a quarter wave of static birefringence, removing the need for the separate quarter-wave plate.

Switching the Pockels cell to its quarter-wave voltage (double-pass retardation equal to half wave) injects a single pulse inside the cavity. The pulse is trapped between the two high reflectors and is amplified for 50 to 500 round trips. The pulse remains in the resonator until the signal from a photodiode that detects light transmitted through one of the end reflectors reaches a predetermined threshold value. A second voltage step is applied to the Pockels cell to cavity dump the amplified pulse.

**Amplification of Nanosecond Pulses from a Narrow-Linewidth Dye Laser**

To obtain very stable frequency output, cw pumping is usually required. The amplification of the low-power output from cw-pumped sources to power levels comparable to those obtained from pulsed solid-state lasers is in many cases desirable. To reach this goal, 5-ns slices from a cw dye laser were amplified in the alexandrite regenerative amplifier. A diagram of the experimental setup is shown in Fig. 34.25.

Fig. 34.25  
Experimental setup for narrow-linewidth regenerative amplification.



Z501

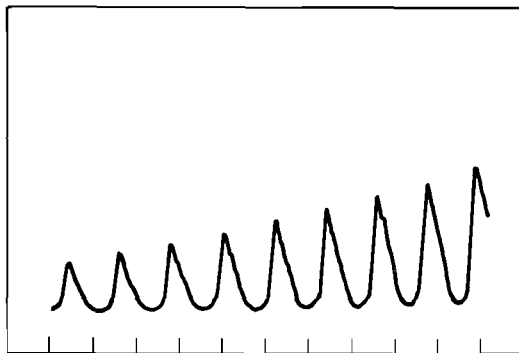
The pulse slicer in Fig. 34.25 is a Pockels cell positioned between two polarizers; it provides a 5-ns transmission window. This device was found necessary since the intracavity Pockels cell does not provide sufficient contrast to prevent some light from the cw laser from leaking into the regenerative amplifier. This leakage forces the laser to operate as an injection-seeded oscillator rather than as a regenerative amplifier. The difference between these two processes is illustrated in Figs. 34.26(a) and 34.26(b). The temporal profile shown in Fig. 34.26(a) is typical of the alexandrite laser operating as a regenerative amplifier. The pulse, which is shorter than the cavity, is shown being amplified at each pass through the resonator, with a total single-pass amplification of 1.06.

If a fraction of the cw dye laser leaks into the resonator for a period longer than the time for a single-cavity round trip, then injection seeding occurs instead of regenerative amplification. In the injection-seeded mode, the pulse is longer than the cavity round-trip time, which creates a standing wave inside the resonator at one (or two) of the resonator modes. The spectrum of the output pulse is then governed by the resonator and is centered at one (or two) of the resonator axial modes. Injection seeding gives a long, smooth pulse buildup, as is shown in Fig. 34.26(b). The addition of the pulse slicer completely eliminates this injection seeding.

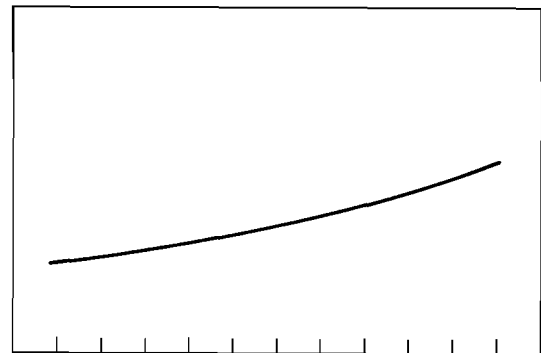
Fig. 34.26

Temporal output from narrow-linewidth regenerative amplifier.

- (a) Light transmitted through one of the end mirrors showing the input pulse being amplified in the resonator.  
 (b) Smooth buildup is observed when the resonator is injection seeded.



(a)  
short-pulse amplification



(b)  
injection seeding

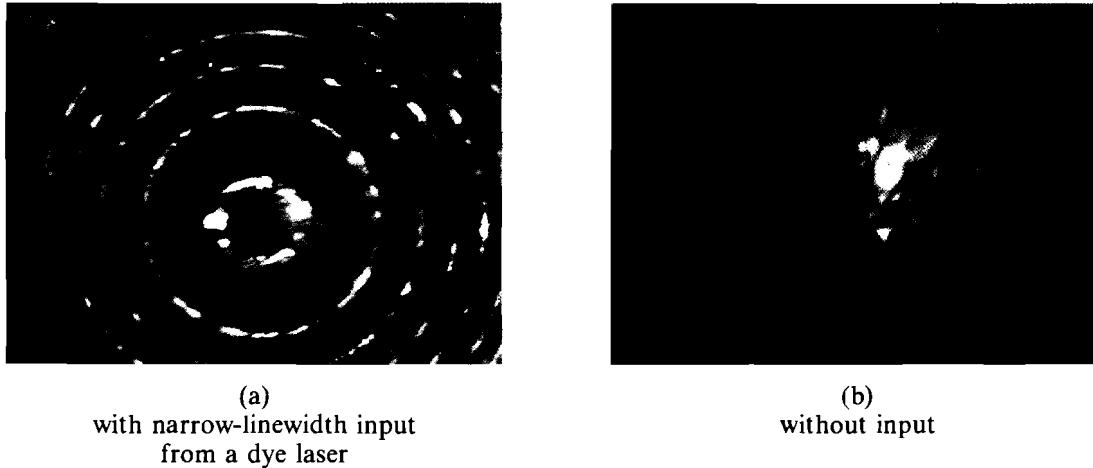
Z502

The temporal pulse output has a pulse duration (FWHM) of approximately 5 ns. The Fourier transform limit for a 5-ns Gaussian pulse is 88 MHz. The spectrum of the amplified pulse as monitored by an air-spaced Fabry-Perot with mirror spacing of 10 cm is shown in Fig. 34.27. The spectral width was measured to be  $100 \pm 15$  MHz.

The input energy of the pulse was approximately 1 nJ, while the output energy is 5 mJ in a clean  $TEM_{00}$  mode. Input energies as low as 10 pJ were amplified. All measurements were done initially at 755 nm, near the peak of the gain curve. When the frequency of the dye

laser is tuned, the output of the regenerative amplifier follows. However, in order to tune far from the gain center of alexandrite, an intracavity broadband tuner, or a more energetic dye laser input than was available, is necessary.

Injection seeding<sup>11,12</sup> is one of the more common alternatives for obtaining reliable narrow-frequency output. This approach requires active feedback, however, and will probably have a lower frequency stability than our technique.



Z503

Fig. 34.27

Spectral output from narrow-linewidth regenerative amplifier from air-spaced Fabry-Perot with 10-cm spacing: (a) with narrow-linewidth input from a dye laser; (b) without input.

#### Amplification of Picosecond Pulses from a Gain-Switched Diode Laser

We have also used our regenerative amplifier to amplify low-energy pulses from a gain-switched laser diode<sup>13</sup> (Sharp, model LT030MD) that lases at 755 nm. Streak-camera measurements of the diode pulse width show that the duration could be varied from 35 to 100 ps by changing the ratio of the RF input to the dc voltage bias. For this experiment, the pulse width was approximately 50 ps, as illustrated in Fig. 34.28.

Typical pulse energies from the diode were 1 pJ. The regenerative amplifier increased the pulse energy by ten orders of magnitude to 10 mJ. Energies as low as 100 fJ could be amplified but somewhat less reliably. The experimental setup was similar to that shown in Fig. 34.25, except that the single-frequency dye laser was replaced by the gain-switched laser diode and a second Faraday rotator and polarizer were also added. The laser diode is quite susceptible to optical damage from amplifier feedback; the two Faraday rotators are necessary to protect the diode. For 10 mJ of output energy, the required alexandrite

flash-lamp input energy was 75 J. Better efficiency could be obtained if one of the end mirrors, which was an 80% reflector, were replaced with a higher reflector. The 80% reflector transmitted sufficient light for diagnostic purposes.

An alternative means of obtaining tunable 10- to 30-ps pulses in the millijoule range is by passively mode-locking alexandrite.<sup>8,14</sup> However, passive mode-locking is inherently noisy, while the regenerative amplification of a well-defined seed pulse can be controlled to a much greater extent. The regenerative amplifier is also more efficient than a passively mode-locked laser. It contains fewer intracavity elements and all the energy is accumulated in a single pulse rather than in a train of pulses.

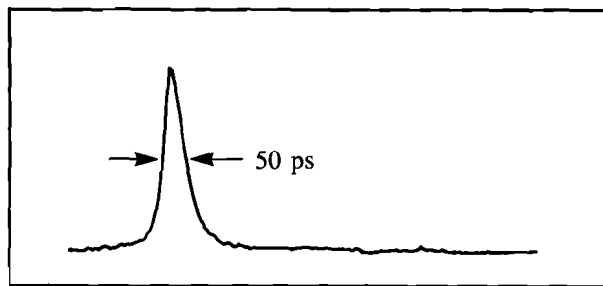


Fig. 34.28  
Temporal pulse shape from gain-switched diode measured with streak camera; FWHM of pulse is  $\sim 50$  ps.

#### Amplification of Femtosecond Pulses from a Synchronously Pumped Dye Laser

Finally, we amplified subpicosecond pulses generated by a synchronously pumped, passively mode-locked dye laser. Traditionally, the amplification of ultrashort pulses has been based on the use of organic dye or excimer amplifiers. These systems offer the broad bandwidths needed to amplify subpicosecond pulses but suffer from low saturation fluences of the order of a few  $\text{mJ}/\text{cm}^2$ . The low saturation fluence restricts the utility of these media to low energy levels—although, in the case of excimer systems, scaling up of the aperture has allowed the generation of pulses approaching a terawatt.

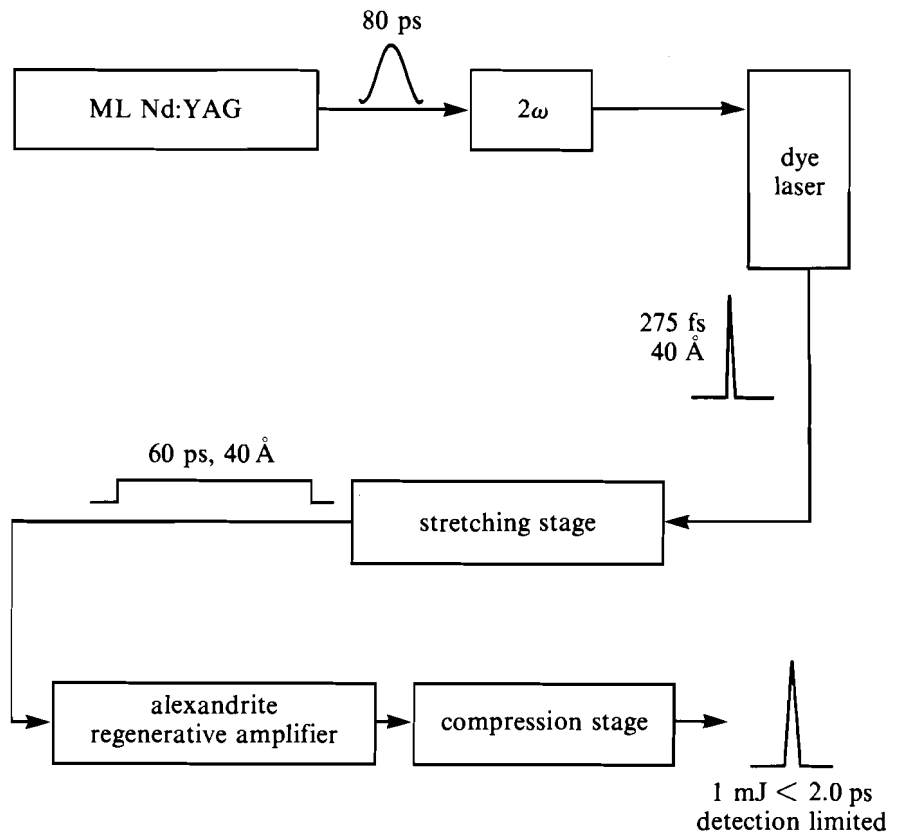
Solid-state media such as Nd:glass or alexandrite have rather large saturation fluences, of the order of 5 to 20  $\text{J}/\text{cm}^2$ . Coupled with their relatively long upper-state lifetimes, these materials have excellent energy storage capabilities. Until recently, however, ultrashort pulses could not take advantage of this capability of solid-state media. The high peak powers produced with subpicosecond pulses can quickly exceed the threshold at which nonlinear effects become significant and distort the spatial and temporal profiles of the pulses. This limits operation to fluence levels well below the saturation fluence. Consequently, the energy extraction efficiency of such systems has traditionally been low.

With the recent development of chirped-pulse amplification,<sup>15</sup> it is now possible to extract efficiently the energy stored in solid-state materials. Briefly, the peak-power limitation is overcome by stretching the pulses prior to amplification. These long pulses can then be amplified to saturation while a relatively low peak power is maintained. After amplification, the pulses are recompressed to their Fourier transform limit.

A schematic of this system is shown in Fig. 34.29. It consists of four subsystems: the dye laser, to provide the seed pulse; a pulse expansion system; the alexandrite regenerative amplifier; and a pulse compression system.

A detailed description of the dye laser is given elsewhere.<sup>16</sup> The dye laser oscillator uses LDS 722 (Pyridine 2) and cryptocyanine as the gain and absorber media, respectively. This laser was pumped by the 850-mW output of a cw mode-locked frequency-doubled Nd:YAG, at a 100-MHz repetition rate.

Fig. 34.29  
Experimental setup for femtosecond-pulse amplification.



Z394

Optimization of the cavity yielded pulses as short as 197 fs. On a day-to-day basis, the dye laser generated 275-fs pulses. Output power of the laser was  $\sim 30$  mW.

Tuning the alexandrite rather than the dye laser allowed us to work with shorter output pulses from the dye laser. A 6- $\mu\text{m}$ -thick pellicle was used inside the alexandrite cavity to tune the peak gain to the dye laser's operating wavelength. Extreme care was taken to mode match the input to the regenerative amplifier cavity, and the alexandrite laser operating wavelength was carefully tuned to coincide with that of the dye laser. Under these conditions, energies as low as 1.0 pJ were sufficient to reliably seed the amplifier. Somewhat higher (5- to 10-pJ) energies were needed if the dye laser was detuned from gain center by  $\sim 5$  nm.

The pulse expansion system consists of two 1800-line/mm gratings in an antiparallel configuration. Between the gratings are two lenses forming a telescope with unit magnification. This grating configuration has previously been shown to provide a net positive GVD.<sup>17,18</sup> A 275-fs, 40- $\text{\AA}$  (FWHM) input pulse to the expansion system is transformed into a positively chirped pulse of 60-ps duration. After expansion, the pulse is amplified in the regenerative amplifier. Finally, a standard double-pass grating compressor can then be used to compress the pulse back to nearly its original duration. If the gratings used in the expansion and compression are identical, the result is a net-zero dispersion to all orders.

Figures 34.30(a)–34.30(c) show the input dye laser spectrum before and after amplification, and the spectrum of the free-running alexandrite laser. There is no evidence of gain narrowing or of any other bandwidth-limiting effects. The output energy at this stage is 2 mJ. Double passing the high-energy chirped pulse through a standard grating compressor yields a streak-camera-limited pulse width of less than 2 ps. In order to realize the full potential that this system holds, we note that at the energies achieved here, the fluence within the amplifier (250 mJ/cm<sup>2</sup>) is still well below the saturation fluence of the medium. Once optimized, this laser source is expected to deliver 20-mJ pulses.

### Conclusion

We have shown that an alexandrite regenerative amplifier is a versatile source capable of amplifying by six to ten orders of magnitude short pulses from various oscillators. The amplifier was used to amplify 5-ns slices from a line-narrowed cw dye laser and 50-ps pulses from a laser diode to the 10-mJ range. We have also combined the technique of chirped-pulse amplification with our alexandrite laser to amplify femtosecond pulses. By using diffraction grating expansion/compression techniques, we have produced subpicosecond pulses with peak powers as high as 2 GW. This source is tunable across a wide bandwidth, limited presently by the dye laser seeding the amplifier, and could serve as a source for continuum generation in the near infrared, or for high field strength studies in atomic physics.



6. J. C. Walling *et al.*, *IEEE J. Quantum Electron.* **QE-16**, 1302 (1980).
7. J. C. Walling *et al.*, *IEEE J. Quantum Electron.* **QE-21**, 1568 (1985).
8. L. Horowitz, P. Papanestor, and D. F. Heller, in *Proc. Int. Conf. Lasers '83*, edited by R. C. Powell (San Francisco, CA, 1985), pp. 550–558.
9. C. Joshi and P. B. Corkum, *Opt. Commun.* **36**, 82 (1981).
10. P. Bado and M. Bouvier, *Rev. Sci. Instrum.* **56**, 1744 (1985).
11. Y. K. Park, G. Giuliani, and R. L. Byer, *IEEE J. Quantum Electron.* **QE-20**, 117 (1984).
12. P. Esherick and A. Owyong, *J. Opt. Soc. Am. B* **4**, 41 (1987).
13. H. Ito, H. Yokoyama, S. Murata, and H. Inaba, *Electron. Lett.* **15**, 738 (1979).
14. V. N. Lisitsyn *et al.*, *Sov. J. Quantum Electron.* **12**, 368 (1982).
15. D. Strickland and G. Mourou, *Opt. Commun.* **56**, 219 (1985).
16. M. Pessot, J. Squier, G. A. Mourou, P. Bado, and D. J. Harter (submitted to *Optics Letters*)
17. O. E. Martinez, *IEEE J. Quantum Electron.* **QE-23**, 59 (1987).
18. M. Pessot, P. Maine, and G. Mourou, *Opt. Commun.* **62**, 419 (1987).

## **Section 3**

# **NATIONAL LASER USERS FACILITY NEWS**

National Laser Users Facility (NLUF) activity during the second quarter of FY88 centered on four activities: the first was the review of proposals received for FY90 research; the second was a series of shots for **U. Feldman** (Naval Research Laboratory); the third was a visit by **C. Hooper** (University of Florida) to discuss analysis of data taken during December 1987; and the fourth was data taken for **C. Collins** (University of Texas).

A total of 13 proposals were received for evaluation by the NLUF Steering Committee. The committee met on 26 February 1988 at LLE. **Dr. B. Arden**, from the University of Rochester, chaired the meeting. Voting members on the 1988 committee are

<b>Dwight Duston</b>	Office of Scientific Development/ Strategic Defense Initiative Office
<b>Damon Giovanielli</b>	Los Alamos National Laboratory
<b>William Kruer</b>	Lawrence Livermore National Laboratory
<b>David Nagel</b>	Naval Research Laboratory
<b>Keith Matzen</b>	Sandia National Laboratory
<b>Eberhard Spiller</b>	IBM Thomas Watson Research Center

The minutes of this meeting have been typed and are being distributed to the committee for approval. Principal investigators will be informed of the results of the evaluation by the middle of April 1988.

**J. Seely** from the Naval Research Laboratory took XUV spectroscopy data during March 1988. Targets of Ge, Pr, W, and Re were irradiated with the OMEGA laser to record XUV spectra. These targets were irradiated with and without the DPP's for intensities of  $6 \times 10^{14}$  and  $5 \times 10^{15}$  W/cm<sup>2</sup>. The Na-like isoelectronic sequence is being studied with these targets.

**C. Hooper**, from the University of Florida, visited on 31 March 1988. He and **M. C. Richardson** of LLE are collaborating on a series on compression experiments using targets of plastic shells filled with Ar, Kr, and Ar/Kr mixtures. Most of the analysis has been centered on an Ar-filled target, where the data indicate a high-density compression. The primary diagnostic for this shot is SPEAXS, a time-dependent crystal spectrograph tuned to the H- and He-like 2p-1s transitions. The data from these shots are being analyzed at both LLE and the University of Florida.

Three shots were taken for **C. Collins** of the University of Texas. He is collaborating with **B. Yaakobi** of LLE on an experiment to use x rays from a laser-generated plasma to excite nuclei. Targets of CaF<sub>2</sub> and CaF<sub>2</sub> overcoated with KCl were used for x-ray spectroscopic measurements.

#### ACKNOWLEDGMENT

This work was supported by the U.S. Department of Energy Office of Inertial Fusion under agreement No. DE-FC08-85DP40200.

## Section 4

# LASER SYSTEM REPORT

### 4.A GDL Facility Report

The GDL laser was in continuous service as a target interaction facility during this quarter. While the system served as an x-ray laser research facility for a majority of its operating time, several campaigns were undertaken in GDL for NLUF users. Active mirrors were in nearly continuous service throughout the period. The GDL beam transported to the OMEGA chamber, called the ALPHA beam, was realigned and reactivated for use in future OMEGA experiments. The ALPHA beam has been newly instrumented with a backscatter monitor and an improved targeting system for more accurate and rapid alignment. Plans for GDL operations for the remainder of the fiscal year include extensive testing of various proposed uniformity improvements for OMEGA.

A summary of GDL operations this quarter follows:

Beamline Test, Calibration, and Tuning Shots	202
Alignment Shots	58
Target Shots	<u>162</u>
TOTAL	422

## 4.B OMEGA Facility Report

The OMEGA laser system was in continuous service this quarter as LLE continued its ultimately successful quest for the 100–200 times liquid DT density milestone. Laser operations subsequent to the achievement of this milestone consisted of recalibration shots for diagnostics and limited exploration of previously successful gas DT target shots.

Throughout January and February, operations personnel assisted in the operation and debugging of the cryogenic target positioner. Assistance was given in eliminating vibration problems, in increasing cryogenic gas flow for improved freezing, in developing better means to diagnose the frozen-layer uniformity, and in general repairs of the cryo positioner.

The laser system continued to provide high-precision performance during this quarter. Beam-energy balance remained consistently in the 3% rms area. The greatly improved illumination uniformity obtained with distributed phase-plate technology and improved polarization control afforded by liquid-crystal circular polarizers contributed to the success of the high-density compression experiments.

The end of the quarter marked the beginning of a planned ten-week period dedicated to laser and target systems maintenance. Following this maintenance period, a characterization period will begin, to test a number of uniformity improvements, to recalibrate the energy measurement system, and to prepare the system for the second phase of cryogenic fuel experiments.

A summary of OMEGA operations for this quarter follows:

Driver Line Shots	63
Beamline Test and Measurement Shots	77
Target Shots	<u>224</u>
TOTAL	364

### ACKNOWLEDGMENT

This work was supported by the U.S. Department of Energy Office of Inertial Fusion under agreement No. DE-FC08-85DP40200 and by the Laser Fusion Feasibility Project at the Laboratory for Laser Energetics, which has the following sponsors: Empire State Electric Energy Research Corporation, New York State Energy Research and Development Authority, Ontario Hydro, and the University of Rochester. Such support does not imply endorsement of the content by any of the above parties.

# PUBLICATIONS AND CONFERENCE PRESENTATIONS

## Publications

A. Simon and R. W. Short, "Comments on 'Motion of an Electron Bunch Through a Plasma'," *Phys. Fluids* **31**, 217 (1988).

H. E. Elsayed-Ali and G. A. Mourou, "Picosecond Reflection High-Energy Electron Diffraction," *Appl Phys. Lett.* **52**, 103-104 (1988).

D. R. Dykaar, R. Sobolewski, J. M. Chwalek, T. Y. Hsiang, and G. A. Mourou, "Electro-Optic Sampler for Characterization of Devices in a Cryogenic Environment," *Advances in Cryogenic Engineering Vol. 33*, edited by R. W. Fast (Plenum, NY, 1988), pp. 1097-1104.

J. S. Wark, R. R. Whitlock, A. Hauer, J. E. Swain, and P. J. Solone, "Short-Pulse X-Ray Diffraction from Laser-Shocked Crystals," *Shock Waves in Condensed Matter 1987*, edited by S. C. Schmidt and N. C. Holmes (Elsevier Science Publishers B. V., 1988), pp. 781-786.

J. F. Whitaker, R. Sobolewski, D. R. Dykaar, T. Y. Hsiang, and G. A. Mourou, "Propagation Model for Ultrafast Signals on Superconducting Dispersive Striplines," *IEEE Trans. Microwave Theory Tech.* **36**, 277-285 (1988).

D. J. Smith, "Modeling of Nodular Defects in Thin Films for Various Deposition Techniques," *Modeling of Optical Thin Films* (SPIE, Bellingham, WA, 1988), Vol. 821, pp. 120-128.

P. A. Jaanimagi, J. Duff, G. G. Gregory, R. L. Keck, M. C. Richardson, W. Seka, D. J. Bowley, S. Majumdar, and J. Wright, "Multi-Channel Optical Streak Cameras," *High Speed Photography*,

*Videography, and Photonics V* (SPIE, Bellingham, WA, 1988), Vol. 832, pp. 236–246.

P. A. Jaanimagi, J. Delettrez, G. G. Gregory, R. S. Marjoribanks, M. C. Richardson, D. K. Bradley, and B. L. Henke, "Application of X-Ray Streak Cameras for Fusion Diagnostics," *High Speed Photography, Videography, and Photonics V* (SPIE, Bellingham, WA, 1988), Vol. 832, pp. 368–375.

G. G. Gregory, P. A. Jaanimagi, P. W. McKenty, S. A. Letzring, and M. C. Richardson, "Precision Alignment Technique for Time-Resolved X-Ray Photography," *High Speed Photography, Videography, and Photonics V* (SPIE, Bellingham, WA, 1988), Vol. 831, pp. 383–391.

D. Shvarts, B. Yaakobi, P. Audebert, T. Boehly, B. Boswell, D. Bradley, R. S. Craxton, R. Epstein, M. C. Richardson, and J. M. Soures, "Studies of New Geometries for X-Ray Laser Experiments," *X Rays from Laser Plasmas* (SPIE, Bellingham, WA, 1988), Vol. 831, pp. 283–292.

R. S. Marjoribanks, M. C. Richardson, P. R. Audebert, D. K. Bradley, G. G. Gregory, and P. A. Jaanimagi, "Time-Resolved Spectroscopy for Detailed Studies ( $\lambda/\Delta\lambda > 1000$ ) of Weak X-Ray Emitters in Laser Plasmas," *X Rays from Laser Plasmas* (SPIE, Bellingham, WA, 1988), Vol. 831, pp. 185–198.

P. C. Cheng, H. Kim, and M. D. Wittman, "Microradiography with Laser-Produced Plasma Sources – Surface Roughness on PMMA Resist," *X Rays from Laser Plasmas* (SPIE, Bellingham, WA, 1988), Vol. 831, pp. 217–223.

P. A. Jaanimagi, G. G. Gregory, S. A. Letzring, R. S. Marjoribanks, and M. C. Richardson, "Time-Resolved Grating Spectrograph Incorporating a Reflection Photocathode for Soft X-Ray Spectroscopy," *X Rays from Laser Plasmas* (SPIE, Bellingham, WA, 1988), Vol. 831, pp. 179–184.

P. Audebert, D. K. Bradley, M. C. Richardson, R. Epstein, P. A. Jaanimagi, O. Barnouin, J. Delettrez, B. Yaakobi, F. J. Marshall, and B. L. Henke, "Time and Space Resolved X-Ray Spectra of Imploding Laser Fusion Targets," *X Rays from Laser Plasmas* (SPIE, Bellingham, WA, 1988), Vol. 831, pp. 9–17.

J. C. Lee, S. D. Jacobs, and R. J. Gingold, "Nd:YAG Laser with Cholesteric Liquid Crystal Cavity Mirrors," *Advances in Nonlinear Polymers and Inorganic Crystals, Liquid Crystals, and Laser Media* (SPIE, Bellingham, WA, 1988), Vol. 824, pp. 7–17.

T. Boehly, P. Audebert, D. Shvarts, B. Yaakobi, B. Boswell, D. Bradley, R. S. Craxton, R. Epstein, M. C. Richardson, and J. M. Soures, "Experimental Studies of New Geometries for X-Ray Laser Experiments," *X Rays from Laser Plasmas* (SPIE, Bellingham, WA, 1988), Vol. 831, pp. 305–320.

W. R. Donaldson, "Optical Probes for the Characterization of Surface Breakdown," *Space Structures, Power, and Power Conditioning* (SPIE, Bellingham, WA, 1988), Vol. 871, pp. 157–164.

R. L. McCrory, "Status of Inertial Confinement Fusion – Panel Discussion," *J. Fusion Energy* **6**, 383–386 (1987).

P. Maine, D. Strickland, P. Bado, M. Pessot, and G. Mourou, "Generation of Ultrahigh Peak Power Pulses by Chirped Pulse Amplification," *IEEE J. Quantum Electron.* **24**, 398-403 (1988).

J. Lambropoulos, "Thermal Stresses During Quenching of Short Glass Cylinders," *J. Am. Ceram. Soc.* **71**, C-24-C-25 (1988).

J. C. Moreno, H. R. Greim, S. Goldsmith, A. Krumbein, R. Epstein, P. A. Jaanimagi, M. C. Richardson, and B. Yaakobi, "Thermal Transport Studies of 351-nm Laser-Produced Plasmas Using Extreme Ultraviolet Spectroscopy," *J. Appl. Phys.*, **63**, 674-680 (1988).

R. Sobolewski, D. R. Dykaar, T. Y. Hsiang, C. Vanneste, and C. C. Chi, "Chaos in Pulse-Driven Josephson Junctions," *Phys. Rev. B.* **37**, 3778-3781 (1988).

G. Mourou, "High Speed Circuit Testing Using Ultrafast Optical Techniques," *Microelectronic Engineering* **7**, 343-349 (1987).

## Forthcoming Publications

The following papers are to be published in the *Proceedings of the 17th Annual Boulder Damage Symposium*, Boulder, CO, October 1985:

K. A. Cerqua, S. D. Jacobs, B. L. McIntyre, and W. Zhong, "Ion Exchange Strengthening of Nd-Doped Phosphate Laser Glass."

B. Liao, D. J. Smith, and B. L. McIntyre, "The Development of Nodular Defects in Optical Coatings."

D. J. Smith, B. Krakauer, C. J. Hayden, A. W. Schmid, and M. J. Guardalben, "Yttrium-Oxide-Based Anti-Reflection Coating for High Power Lasers at 351 nm."

---

G. Mourou, "Picosecond Electro-Optic Sampling," to be published in the *Proceedings of the High Speed Electronics Conference*, Stockholm, Sweden, August 1986.

R. L. McCrory and J. M. Soures, "Inertially Confined Fusion," to be published in *Applications of Laser Plasmas*, Chapter 7.

K. A. Cerqua, J. Hayden, and W. C. LaCourse, "Stress Measurements in SOL-GEL Films," to be published in the *Journal of Non-Crystalline Solids*.

P. C. Cheng, H. Kim, D. M. Shinozaki, K. H. Tan, and M. D. Wittman, "X-Ray Microscopy - Its Application to Biological Sciences," to be published in the *Proceedings of the X-Ray Microscopy Meeting '87*, Stony Brook, NY, September 1987 (Springer-Verlag).

K. L. Marshall and S. D. Jacobs, "Near-Infrared Dichroism of a Mesogenic Transition Metal Complex and Its Solubility in Nematic Hosts," to be published in *Molecular Crystals and Liquid Crystals*.

W. Watson, "Vacuum-Assisted Contaminated Particulate Removal," to be published in the *Journal of Vacuum Science and Technology*.

K. A. Cerqua, M. J. Shoup III, D. L. Smith, S. D. Jacobs, and J. H. Kelly, "Strengthened Phosphate Glass in a High Rep Rate Active-Mirror Amplifier Geometry," to be published in *Applied Optics*.

B. Yaakobi, D. Shvarts, T. Boehly, P. Audebert, R. Epstein, B. Boswell, M. C. Richardson, and J. M. Soures, "X-Ray Laser Studies at LLE," to be published in *IEEE Transactions in Plasma Physics*.

D. R. Dykaar, J. Chwalek, J. F. Whitaker, R. Sobolewski, T. Y. Hsiang, G. A. Mourou, D. K. Lathrop, S. E. Russek, and R. A. Buhrman, "High Frequency Characterization of Thin-Film Y-Ba-Cu Oxide Superconducting Transmission Lines," to be published in *Applied Physics Letters*.

R. Q. Gram, C. K. Immesoete, H. Kim, and L. Forsley, "Bounce-Coated Ablation Layers on Fusion Targets," to be published in the *Journal of Vacuum Science and Technology*.

P. Maine and G. Mourou, "Amplification of 1 ns Pulses in Nd:Glass Followed by Compression to 1 ps," to be published in *Optics Letters*.

P. C. Cheng, S. P. Newberry, H. Kim, and M. D. Wittman, "X-Ray Contact Microradiography and Shadow Projection X-Ray Microscopy," to be published in the *European Journal of Cell Biology*.

W. R. Donaldson, "Radial Line Structure Experiments," to be published in the *Proceedings of the 4th Workshop: Pulse Power Techniques for Future Accelerators*, Erice, Sicily, 3-10 March 1988.

## Conference Presentations

The following presentations were made at SPIE's OE-LASE '88, Los Angeles, CA, 10-17 January 1988:

S. D. Jacobs, K. A. Cerqua, K. L. Marshall, A. Schmid, M. J. Guardalben, and K. J. Skerrett, "Liquid Crystal Optics for Laser Systems."

M. C. Richardson, P. A. Jaanimagi, H. Chen, R. S. Marjoribanks, D. K. Bradley, J. F. Seely, U. Feldman, C. Brown, J. Underwood, and B. Henke, "Space- and Time-Resolved Diagnostics of Soft X-Ray Emission from Short-Pulse Laser Plasmas."

R. L. McCrory, J. M. Soures, C. P. Verdon, P. Audebert, D. Bradley, J. Delettrez, R. Hutchison, S. D. Jacobs, P. Jaanimagi, R. Keck, H. Kim, T. Kessler, J. Knauer, R. Kremens, S. Letzring, F. Marshall, P. McKenty, M. C. Richardson, A. Simon, R. Short, S. Skupsky, and B. Yaakobi, "High-Pressure Laser-Fusion Compression Results."

B. Yaakobi, D. Shvarts, T. Boehly, P. Audebert, R. Epstein, B. Boswell, M. C. Richardson, and J. M. Soures, "X-Ray Laser Studies at LLE."

P. Maine, D. Strickland, and G. Mourou, "Tabletop Terawatt Laser by Chirped Pulse Amplification."

W. R. Donaldson, "Optical Probes for the Characterization of Surface Breakdown."

---

G. Mourou, "Future Applications of High Tc Superconductors in High Speed Electronics and Communications," presented at the World Conference on Superconductivity, Houston, TX, 21-24 February 1988.

W. R. Donaldson, "Radial Line Structure Experiments," presented at the 4th Workshop: Pulse Power Techniques for Future Accelerators, Erice, Sicily, 3-10 March 1988.

---

The following presentations were made at the 7th Topical Conference on High Temperature Plasma Diagnostics, Napa, CA, 13-17 March 1988:

P. A. Jaanimagi, D. K. Bradley, J. Duff, G. G. Gregory, and M. C. Richardson, "Time-Resolving X-Ray Diagnostics for ICF" (invited paper).

M. C. Richardson, D. K. Bradley, P. A. Jaanimagi, J. Delettrez, R. Epstein, C. F. Hooper, R. C. Mancini, and D. Kilcrease, "X-Ray Diagnosis of High Density Compression of Ar-Filled Polymer Shell Targets."

---

The following presentations were made at SPIE's Advances in Semiconductors and Superconductors: Physics and Device Applications Conference, Newport Beach, CA, 13-18 March 1988:

G. Mourou, D. Dykaar, J. Chwalek, and J. Whitaker, "High-Temperature Superconductors for High-Speed Interconnects and Communications."

G. Mourou, D. Dykaar, J. Whitaker, and K. Meyer, "Ultrafast Optics for High Speed Electronics."

#### ACKNOWLEDGMENT

The work described in this volume includes current research at the Laboratory for Laser Energetics, which is supported by Empire State Electric Energy Research Corporation, New York State Energy Research and Development Authority, Ontario Hydro, the University of Rochester, and the U.S. Department of Energy Office of Inertial Fusion under agreement No. DE-FC08-85DP40200.